A&A 386, 12–30 (2002)
DOI: 10.1051/0004-6361:20020226

Astronomy
&
Astrophysics

Lens magnification by CL0024+1654 in the U and R band

S. Dye[1], A. N. Taylor[2], T. R. Greve[3,4], Ö. E. Rögnvaldsson[5], E. van Kampen[2], P. Jakobsson[6], V. S. Sigmundsson[6], E. H. Gudmundsson[6], and J. Hjorth[3]

[1] Astrophysics Group, Blackett Laboratory, Imperial College, Prince Consort Road, London SW7 2BW, UK
[2] Institute for Astronomy, University of Edinburgh, Royal Observatory, Blackford Hill, Edinburgh EH9 3HJ, UK
[3] Astronomical Observatory, Juliane Maries Vej 30, 2100 Copenhagen Ø, Denmark
[4] Department of Physics & Astronomy, University College London, Gower Street, London WC1E 6BT, UK
[5] NORDITA, Blegdamsvej 17, 2100 Copenhagen Ø, Denmark
[6] Science Institute, Dunhaga 3, 107 Reykjavik, Iceland

Received 28 August 2001 / Accepted 8 February 2002

Abstract. We estimate the total mass distribution of the galaxy cluster CL0024+1654 from the measured source depletion due to lens magnification in the R band. Within a radius of $0.54\,h^{-1}$ Mpc, a total projected mass of $(8.1 \pm 3.2) \times 10^{14}\ h^{-1}\ M_\odot$ (EdS) is measured. The 1σ error here includes shot noise, source clustering, uncertainty in background count normalisation and contamination from cluster and foreground galaxies. This corresponds to a mass-to-light ratio of $M/L_B = 470 \pm 180$. We compute the luminosity function of CL0024+1654 in order to estimate contamination of the background source counts from cluster galaxies. Three different magnification-based reconstruction methods are employed: 1) an estimator method using a local calculation of lens shear; 2) a non-local, self-consistent method applicable to axi-symmetric mass distributions; 3) a non-local, self-consistent method for derivation of 2D mass maps. We have modified the standard single power-law slope number count theory to incorporate a break and applied this to our observations. Fitting analytical magnification profiles of different cluster models to the observed number counts, we find that CL0024+1654 is best described either by a NFW model with scale radius $r_{\rm s} = 334 \pm 191\,h^{-1}$ kpc and normalisation $\kappa_{\rm s} = 0.23 \pm 0.08$ or a power-law profile with slope $\xi = 0.61 \pm 0.11$, central surface mass density $\kappa_0 = 1.52 \pm 0.20$ and assuming a core radius of $r_{\rm core} = 35\,h^{-1}$ kpc. The NFW model predicts that the cumulative projected mass contained within a radius R scales as $M(<R) = 2.9 \times 10^{14} (R/1')^{1.3-0.5\,\lg(R/1')}\ h^{-1}\ M_\odot$. Finally, we have exploited the fact that flux magnification effectively enables us to probe deeper than the physical limiting magnitude of our observations in searching for a change of slope in the U band number counts. We rule out both a total flattening of the counts with a break up to $U_{\rm AB} \leq 26.6$ and a change of slope, reported by some studies, from ${\rm d}\log N/{\rm d}m = 0.4 \rightarrow 0.15$ up to $U_{\rm AB} \leq 26.4$ with 95% confidence.

Key words. gravitational lensing – galaxies: clusters: individual: CL0024+1654 – cosmology: dark matter

1. Introduction

The lensing cluster CL0024+1654 ranks as one of the most highly studied clusters to date. Lying at a redshift of $z = 0.39$, early measurements of the cluster's velocity dispersion of $\sigma \simeq 1300 \pm 100$ km s^{-1} (Dressler et al. 1985) suggested a formidable mass. The discovery of a large gravitationally lensed arc from a blue background galaxy by Koo (1988) has since provoked a range of studies to estimate the cluster's mass based on its lensing properties.

The first lens inversion of CL0024+1654, by Kassiola et al. (1992), noted a violation of the "length theorem" (Kovner 1990) that the length of the middle segment of the arc should equal the sum of the other two. The authors demonstrated that a concentration of large cluster galaxies near the arc centre is necessary to cause this by perturbing the cluster cusp and were thus able to constrain the potential of the cluster and the perturbing galaxies. A later analysis by Bonnet et al. (1994) constrained the cluster's mass profile more tightly with the first measurement of weak shear out to a radius of $1.5\,h^{-1}$ Mpc. Wallington et al. (1995) confirmed the perturbing galaxy hypothesis of Kassiola et al. by fitting a smooth elliptical cluster potential with two superimposed L_* galaxy potentials near the centre of the arc.

By parameterising the source and lens models and fitting to six images of the lensed source galaxy, Kochanski et al. (1996) again showed that the mass profile of CL0024+1654 is consistent with a smooth isothermal distribution. Furthermore, they found that the cluster mass traces light fairly well out to a radius of $0.5\,h^{-1}$ Mpc and were able to rule out the existence of any significant

---

Send offprint requests to: S. Dye,
e-mail: `sdye01@ic.ac.uk`

substructure larger than $15\,h^{-1}$ kpc in the central region. Using HST images of the cluster, Tyson et al. (1998, TKD hereafter) isolated eight well-resolved images of the blue background galaxy to construct a high resolution mass map of the cluster. Their parametric inversion concluded that more than 98% of the mass concentration excluding that contributed from discrete galaxies was represented by a smooth distribution of mass with a shallower profile than isothermal.

The most recent lensing analysis of CL0024+1654 to date is that by Broadhurst et al. (2000, B00 hereafter) who provide the first measurement of the redshift of the blue background galaxy at $z = 1.675$. This redshift breaks the mass-redshift degeneracy present in all mass estimates of the cluster thus far. Their fit of NFW profiles (Navarro et al. 1997) to the eight brightest cluster members is found to be an adequate model to explain the positions of the five main lensed images. This, they suggest, highlights the possibility that sub-structure has not been erased in the cluster.

The first of only two measurements of the cluster's lens magnification to currently exist was that investigated by Fort et al. (1997). This was the first detection of depletion in background galaxy number counts due to geometrical magnification as predicted by Broadhurst et al. (1995, BTP hereafter). Rather than reconstruct cluster mass, this work concentrated on characterising the radial distribution of critical lines to infer the redshift range of the background populations in B and I. Using this data, van Kampen (1998) produced an estimate of the mass of CL0024+1654 from lens magnification.

The only other magnification analysis of the cluster published so far is that of Rögnvaldsson et al. (2001; R01 hereafter) using R and U band observations. Their choice to observe in U was inspired by the findings of Williams et al. (1996) which suggested a flattening in the U band number count slope at faint magnitudes. Such a break is reported to occur at $U_{\rm AB} \simeq 25.5{-}26$ with a change of slope of $\mathrm{d}\log N/\mathrm{d}m \simeq 0.4 \rightarrow 0.15$. Given suitably deep U band imaging, this should therefore manifest itself as a depletion in the number density of galaxies observed in the presence of lens magnification (see Sect. 3.2). R01 claimed to have detected depletion in U implying that a break in the slope must be present.

Further investigation has since highlighted concern regarding the reliability of faint objects extracted by R01 from the R and U band observations. While this is not a large concern for R where the depletion signal is strong, the claim of detection of depletion in U and hence the reported break in the number count slope is strongly affected. A re-examination of these findings is therefore necessary.

The motivation driving the paper presented here is severalfold. Firstly, there is the need to re-evaluate the existing results of R01. We take the observations from R01 but create new, more reliable R and U band object catalogues. Using these, we re-calculate the depletion signal in both bands and use this to re-fit the isothermal lens model of R01. Secondly, we wish to extend the analysis of R01: 1) We fit a power-law profile and a NFW model to the depletion profiles. 2) We transform the measured depletion into mass estimates using three recently developed magnification reconstruction methods; the local estimator method of van Kampen (1998) applied by Taylor et al. (1998, T98 hereafter), the non-local axi-symmetric solution of T98 for reconstruction of radial mass profiles and the non-local method of Dye & Taylor (1998) for determining 2D mass maps. 3) We investigate the relationship between mass, light and galaxy number density in the cluster. 4) We quantify contamination of our background source sample by cluster and foreground objects and incorporate this into our analyses. 5) Finally, we apply two methods to search for a change in slope in the U band field galaxy number counts by exploiting the fact that lens magnification enables us to effectively see deeper than the physical magnitude limit imposed by the observations.

The following section briefly describes data acquisition, reduction, object extraction and mask generation. Contamination of the source counts from cluster and foreground galaxies is estimated. Section 3 details the reconstruction methods used in this paper. In Sect. 4, we consider the properties of the R band background galaxy population and fit cluster mass models to the measured number count profile. This is necessary for determination of the mass results presented in Sect. 5. In Sect. 6, we investigate the U band galaxy population and test for the existence of a break in the number counts. Finally, we discuss and summarise our findings in Sect. 7.

2. The data

Data acquisition and reduction are described in full detail in R01. Here, we highlight the key deviations in the generation of the object catalogues of this paper from those in R01:

- a Gaussian smoothing kernel with a *FWHM* equal to the seeing was used to extract objects (see Sect. 2.2). This compares with the narrower smoothing kernel of *FWHM* equal to slightly larger than half the seeing used by R01 (note the incorrect statement that their smoothing kernel is equal to the seeing). Matching the width of the smoothing kernel to the seeing allows optimal extraction in the sense that spurious detections due to background noise are kept as small as possible while maintaining a sufficiently large detection success rate. This creates the most noticeable difference between this dataset and that of R01; our U and R catalogues contain fewer faint objects (our total paired object catalogue contains 29% fewer objects);
- galactic extinction corrections have been applied to both the U and R band, brightening all objects (see Sect. 2.1);
- a more thorough determination of the background noise has been obtained. The mean rms background variation has been calculated within a circular

aperture of diameter equal to the seeing *FWHM*. The result of this is that the "3σ" detection limits calculated in R01 from Poisson statistics are fainter than those in this paper by 1.3 mag in U and 1.7 mag in R including the galactic extinction correction;

- a linear co-ordinate transformation has been applied to the U band object positions resulting in a more accurate mapping to the R band. This has improved the position coincidence matching between both bands.

2.1. Acquisition and completeness

CL0024+1624 was observed in the Cousins U and Cousins R bands with a $6' \times 6'$ field of view using the Nordic Optical Telescope in August 1999. A total integration time of 37 ks and seeing $1.1''$ was obtained in the U band compared with 8.7 ks and $1.0''$ in the R. Following R01, we use AB magnitudes throughout this paper converting from the Cousins U and R magnitudes with an offset of +0.71 mag and +0.20 mag respectively (Fukugita et al. 1995). In addition, we have corrected the data for galactic extinction amounting to −0.15 mag and −0.31 mag in the R and U band respectively (Schlegel et al. 1998). The limiting magnitudes corresponding to a signal-to-noise ratio of 3 within a seeing disk are $U_{\rm AB} = 25.7$ mag and $R_{\rm AB} = 25.8$ mag, with the noise level taken as the mean rms of the background. All photometry was performed using SExtractor (Bertin & Arnouts 1996; see Sect. 2.2). Magnitudes were measured as either total or corrected isophotal depending on the proximity of neighbouring objects. This is managed automatically via SExtractor's `MAG_BEST` magnitude definition.

Completeness was estimated from the detectability of synthetic objects of varying brightness added to the images. Further details can be found in R01. In re-applying this process to the data of this paper, we find that the completeness at the 3σ detection limit is 84% at $U_{\rm AB} = 25.7$ mag and 81% at $R_{\rm AB} = 25.8$ mag.

2.2. Object extraction

Objects were extracted from the final reduced images using SExtractor. With a detection threshold of 1σ above background and a Gaussian filtering kernel of *FWHM* equal to the seeing, catalogues of all objects with at least 10 connecting pixels brighter than the threshold were generated. A total of 1887 objects in the R band and 1122 objects in the U band were detected. These totals include stars but exclude objects classified by SExtractor as having saturated pixels, being truncated or possessing corrupt isophotal data. By matching the 30 brightest stars between both bands, a linear co-ordinate transformation was calculated and applied to map the U band catalogue onto the R band. Objects were paired within a positional tolerance equal to the seeing and yielded a total of 875 objects excluding stars. Those objects with star/galaxy classification indices larger than 0.95 were assumed to be stars and excluded from the analysis below.

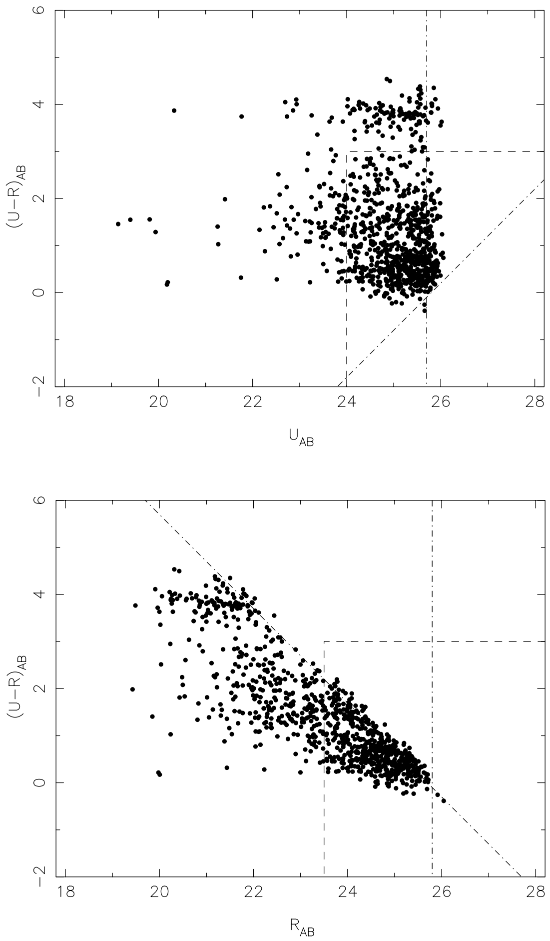

Fig. 1. Colour-magnitude diagrams for all 875 matched objects. Top and bottom shows selection of mask objects in the U and R band respectively by the criteria $(U-R)_{\rm AB} > 3$ and $U_{\rm AB} < 24$, $R_{\rm AB} < 23.5$ (dashed lines). The 3σ detection limits $U_{\rm AB} = 25.7$ and $R_{\rm AB} = 25.8$ are shown in both plots by the dot-dashed lines.

2.3. Object selection

Separation of the background galaxies from the foreground and cluster galaxies must be achieved before lens magnification can be evaluated. Segregation of the cluster and foreground objects is important to enable estimation of their background sky obscuration which affects binned number counts.

Figure 1 shows the colour-magnitude plot of $(U-R)_{\rm AB}$ versus the $U_{\rm AB}$ and $R_{\rm AB}$ magnitudes for the 875 matched objects. By matching our sample with the redshift measurements of the field of CL0024+1654 by Czoske et al. (2001b), we have found that a large fraction of cluster members can be immediately discarded by removing objects with $(U-R)_{\rm AB} > 3$. The noticeable lack of objects seen in the vicinity of $(U-R)_{\rm AB} \simeq 3$ reflects a minimum in the bi-modal $(U-R)$ distribution of cluster galaxies identified in the Czoske et al. sample by the criterion $0.388 < z < 0.405$. Applying a further selection $R_{\rm AB} < 22$ to avoid incompleteness in both the Czoske et al. sample and our data, we find that 65% of identified cluster objects

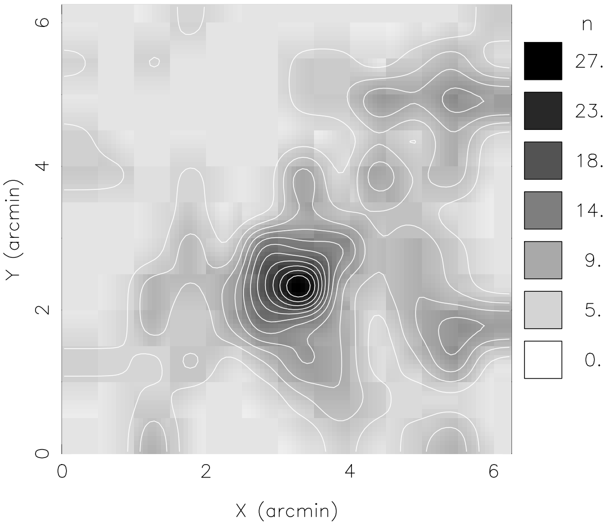

Fig. 2. Number density (n = number/square arcmin) of cluster galaxies selected either by $(U-R)_{\rm AB} > 3$ or redshift.

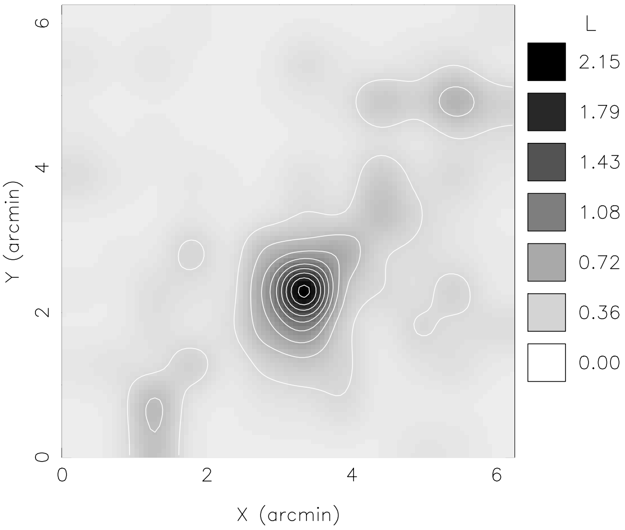

Fig. 3. Distribution of light (surface flux density L converted to the restframe B band and expressed in units of $10^{13}\ L_\odot\ {\rm Mpc}^{-2}\,h^2$) from cluster galaxies selected either by $(U-R)_{\rm AB} > 3$ or redshift. Contours are separated by equal flux intervals.

lie at $(U-R)_{\rm AB} > 3$. In addition, we find that 12% of objects brighter than $R_{\rm AB} = 22$ with $(U-R)_{\rm AB} > 3$ are foreground galaxies and only 2% of objects in this selection are background objects. In summary, the selection $(U-R)_{\rm AB} > 3$ very efficiently removes cluster galaxies, at least up to $R_{\rm AB} = 22$, discarding a very small fraction of background sources.

In Fig. 2, we plot the number density of cluster galaxies defined as objects with colour $(U-R)_{\rm AB} > 3$ or by their redshift for $(U-R)_{\rm AB} < 3$. Figure 4 shows how the number counts of galaxies meeting these criteria vary with magnitude in the U and R. In Fig. 3 we plot the distribution of light from these selected cluster galaxies. The surface flux density shown in this plot is scaled to the restframe B band for easy comparison of the mass-to-light ratio we calculate later with other authors. This scaling was carried out using the K and colour corrections presented in Fukugita et al. (1995). Both distributions are compared with the reconstructed cluster mass map in Sect. 5.1. The fact that both distributions are relatively concentrated around the known cluster centre indicates that we have reliable selection criteria for the (bright) cluster members.

Our foreground and cluster objects are therefore chosen as a combination of objects identified in the Czoske et al. sample with $z < 0.405$ as well as those satisfying $(U-R)_{\rm AB} > 3$ and an additional $R_{\rm AB} < 23.5$ for the R band sample or an additional $U_{\rm AB} < 24.0$ for the U band sample. The choice of R and U limits here are chosen to be optimal in the sense that they select as many background objects as possible while preventing too high a degree of contamination from cluster and foreground objects (see Sect. 2.4). Extracted parameters such as size, ellipticity and orientation of the cluster and foreground objects are used to generate an obscuration mask as Sect. 2.5 details.

Rather than perform our analyses on the associated object catalogue (i.e. containing only objects with paired U and R mags) which would miss faint objects detected in only either the U or R band, we take our background source list for each band from the individual complete U and R catalogues. To obtain our source list, we remove objects from each complete catalogue identified as cluster members and foreground objects using the colour-magnitude and redshift criteria above.

For our U band break analysis in Sect. 6, removal of contaminants causes a slight dilemma. Although we would like our U band sample to be contamination free so that any lensing signal present is maximised, we also wish to remain consistent with existing U band studies to prevent our search for the break from being biased in some way. It turns out that since the Czoske et al. redshift survey extends to only relatively shallow U band magnitudes, we only identify and remove 5 foreground objects which fall within the colour-magnitude selection criteria for our background sample. We have therefore introduced only a negligible inconsistency with other U band number count studies and yet have removed all we can in terms of known foreground objects. We know that there are more foreground objects in our background sample than we have been able to remove (see Sect. 2.4.1) so we are forced to allow for these as a contamination error in our lensing analysis. As far as removal of objects with $(U-R)_{\rm AB} > 3$ is concerned, this simply removes the majority of surplus cluster galaxies which aren't present in published number count studies anyway.

In the R band, this does not pose a problem. We do not have to ensure that our R band data is consistent with any other sample since our depletion is normalised to counts near the edge of the field rather than independent measurements. Removal of as many foreground and cluster objects as possible is therefore the ideal. As with the U band sample, we can not achieve this fully so must resort

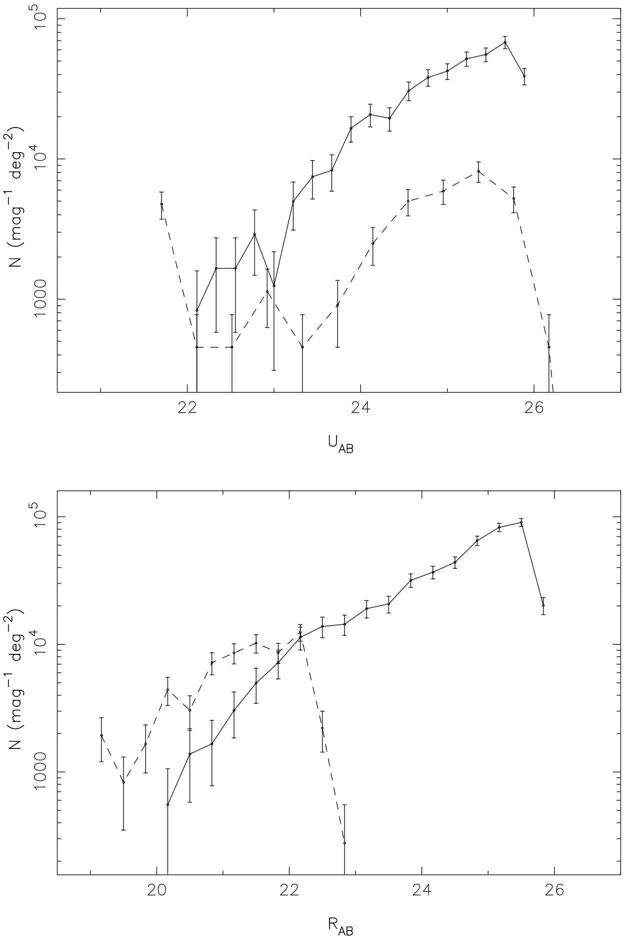

Fig. 4. Number counts as a function of magnitude for the U band (top) and R band (bottom). Plotted are counts of galaxies in the background sample (solid) and cluster galaxies (dashed). Errors account for shot noise only.

to treating the remainder as a source of error in the mass reconstructions.

After removal of cluster and foreground objects from our full U and R catalogues, we find a total of 863 background galaxies remaining in the U and 1367 in the R. Figure 4 plots the number counts of both these samples as a function of magnitude. Notice how the U band counts are significantly steeper than in R. All subsequent magnification analysis will be performed on these two catalogues.

2.4. Contamination of background source samples

We discussed in the previous section that ∼65% of cluster galaxies lie at $(U-R)_{\rm AB} > 3$ for $R_{\rm AB} < 22$. For the R band sample, this does not provide a useful means of removing cluster galaxies as the background source selection limit of $R_{\rm AB} \geq 23.5$ prevents inclusion of objects with $(U-R)_{\rm AB} > 3$ anyway due to the U band detection limit of $U_{\rm AB} = 25.7$. By including objects from the full R band catalogue, faint objects with $(U-R)_{\rm AB} > 3$ will inevitably fall into the background R sample. Additionally, the cluster galaxies which lie at $(U-R)_{\rm AB} < 3$ will contaminate both U and R samples along with any foreground galaxies. This contamination must be quantified.

2.4.1. Foreground galaxy contamination

To estimate the foreground galaxy contamination expected within our chosen magnitude ranges, we use the luminosity functions measured by the CNOC2 field galaxy redshift survey (Lin et al. 1999). The CNOC2 survey is ideal for our purposes being the largest intermediate redshift survey to date with multicolour $UBVRI$ photometry.

The number of objects N which exist within the apparent magnitude range $m_1 < m < m_2$ and the redshift range $z_1 < z < z_2$ can be estimated as

$$N = \int_{z=z_1}^{z=z_2} {\rm d}V(z) \int_{M_1(z)}^{M_2(z)} \phi(M)\,{\rm d}M \qquad (1)$$

where ${\rm d}V(z)$ is the comoving volume element, $\phi(M)$ is the luminosity function and the absolute magnitudes $M_1(z)$ & $M_2(z)$ correspond to the apparent magnitudes m_1 and m_2 at a redshift z. The fraction of objects which lie closer than a redshift z_f in a sample of galaxies observed within the magnitude range $m_1 < m < m_2$ is therefore given by,

$$\frac{N(m_1 < m < m_2, z < z_f)}{N(m_1 < m < m_2)}. \qquad (2)$$

The denominator here is the total number of galaxies within $m_1 < m < m_2$ integrated over all redshifts. Using this equation, we estimate the fraction of galaxies within our U and R background samples lying at $z < 0.405$, allowing for an early+intermediate mixed galaxy K-correction (Fukugita et al. 1995) for the magnitudes in Eq. (1).

We use the early+intermediate (Cousins) R and (Cousins) U luminosity functions from the CNOC2 survey for calculation of N in Eq. (1). These predict that the contamination due to foreground galaxies is 3% in the U band sample and 2% in the R band assuming an EdS cosmology. For the case $\Omega = 0.3$, $\Lambda = 0.7$, these fractions drop only very slightly. We find that this result is insensitive to the choice of K-correction mix.

2.4.2. Cluster contamination and the cluster luminosity function

To determine the cluster contamination fraction, we need to be able to predict the number of cluster members expected within the magnitude range spanned by the selection magnitude and the detection limit in both bands. This requires knowledge of the cluster luminosity function (CLF) for CL0024+1654.

We fit our own CLF to the cluster counts determined by matching with the Czoske et al. cluster members (see Sect. 2.3) in both the U and R. We use the likelihood method of Sandage et al. (1979) and check the consistency of our results with several published CLFs. In the R band, we compare with three recent studies of the

Table 1. Schechter parameters of the CLF/CCLFs used for estimation of cluster contamination, C, expressed as the percentage of objects expected to be cluster members within $23.5 < R_{\rm AB} < 25.5$ for r or $24.0 < U_{\rm AB} < 25.5$ for $U_{\rm c}$. Note that the contamination fractions calculated from the CLFs of this work are weighted averages (see text).

CLF/CCLF	Band	M_*	α	C (%)
Paolillo CCLF	r	-22.2	-1.01	15
Piranomonte CCLF	r	-22.0	-0.91	13
Garilli CCLF	r	-22.1	-0.60	5
This work CLF	r	-21.9	-0.70	19
Beijersbergen CLF	$U_{\rm c}$	-19.4	-1.54	8
This work CLF	$U_{\rm c}$	-21.5	-1.41	9

composite CLF (CCLF): Paolillo et al. (2001) who construct a CCLF from 39 Abell clusters, Piranomonte et al. (2000) whose CCLF is constructed from 86 Abell clusters and Garilli et al. (1999) who use 65 Abell and X-ray selected clusters to calculate a CCLF. All three studies use observations in the Gunn r filter so we must apply a K-colour-correction for the absolute magnitude conversion $M_{R_{\rm AB}} \rightarrow M_r$. Since ∼60−70% of galaxies within clusters are E/S0 types (Dressler et al. 1997; see also Smail et al. 1997 for specific case of CL0024+1654), we calculate this correction using an elliptical galaxy spectrum taken from Kinney et al (1996).

In the U band, publications on CLFs are rare and there are no known U band CCLFs to date. Applying K-colour-corrections to convert redder-band magnitudes to the U band when the galaxy type mix is not known accurately is not reliable. We therefore choose the most heavily studied cluster in the U band, the Coma cluster, and compare our fit with the CLF from the recent study by Beijersbergen et al. (2001). In a similar manner to the R band, we apply a correction to take absolute $U_{\rm AB}$ magnitudes at $z = 0.39$ to rest-frame absolute Cousins U magnitudes.

Figure 5 plots the various CLFs/CCLFs, all of which are described by a Schechter function (Schechter 1976) with parameters given in Table 1. For the r band CCLF from each study, we have taken Schechter parameters corresponding to the rich subsample of clusters for consistency with CL0024+1654. All luminosity functions are normalised to our cluster counts which are superimposed in both plots. Absolute magnitudes assume $q_0 = h_0 = 0.5$. For correct normalisation, we must ensure that the Czoske et al. matched sample for each band does not suffer from incompleteness. We therefore limit the matched U band counts to the magnitude range $21.8 < U_{\rm AB} < 24.0$ ($-22.4 < M_U < -20.2$) and the matched R band counts to $19.9 < R_{\rm AB} < 22.1$ ($-23.3 < M_r < -21.1$).

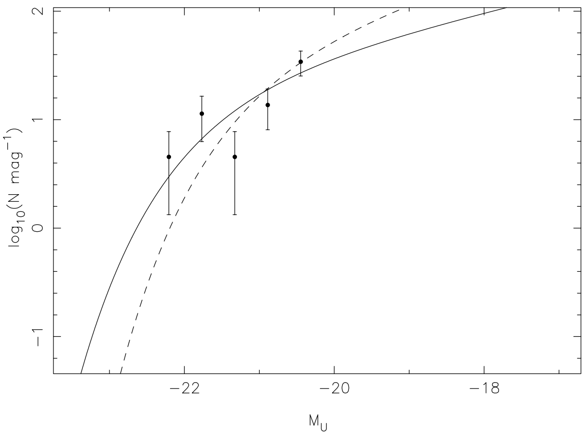

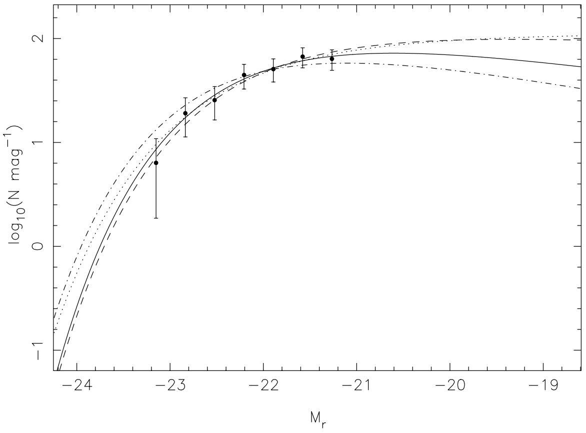

Fig. 5. Luminosity functions of CL0024+1654 galaxies. *Top*: U band Schechter LF from Beijersbergen et al. (2001) for the Coma cluster (dashes) and the best fit LF determined in this work (solid). *Bottom*: r band CCLFs for rich clusters from Paolillo et al. (2001, dots), Piranomonte et al. (2000, dashes), Garilli et al. (1999, dot-dashes) and the best fit from this work (solid).

Integrating over each of the CLFs/CCLFs, we are able to calculate the number of cluster galaxies expected. For the published luminosity functions presented here, this is a straight-forward integral. For our own fitted CLFs however, we incorporate the uncertainty arising from their fit to obtain a more fair level of contamination. We calculate the number of cluster galaxies as

$$n_{\rm c} = A \left\langle \phi^*(M_*, \alpha) \int_{M_{\rm a}}^{M_{\rm b}} {\rm d}M \phi(M; M_*, \alpha) \right\rangle_{M_*, \alpha} \qquad (3)$$

where the angular brackets denote averaging over each realisation of M_* and α weighted by the corresponding probability from the CLF fit. A is a normalisation constant calculated as the inverse of the sum of these probabilities. The absolute magnitudes $M_{\rm a}$ and $M_{\rm b}$ correspond to the apparent magnitude ranges $23.5 < R_{\rm AB} < 25.5$ for r or $24.0 < U_{\rm AB} < 25.5$ for $U_{\rm c}$. These ranges are chosen to extend slightly less deep than the 3σ detection limits, allowing comparison with a more complete background sample to give a more accurate estimation of contamination.

Within the appropriate magnitude ranges given above, the last column of Table 1 lists the predicted number of cluster galaxies as a percentage of the total number of galaxies detected. In R, the estimated contamination from the published luminosity functions ranges between

5% and 15%. The weighted average predicted contamination from our own R band CLF is higher at 19%. In the U band, the contamination levels are not as high since the known Czoske cluster galaxies have been discounted in the calculation. We find that the Coma CLF predicts that 8% of objects in our background sample are cluster objects, compared with our CLF which gives a weighted average of 9%.

The total contamination predicted from both foreground and cluster galaxies therefore has a relatively wide spread in the R band of 7% to 21% compared to between 11% and 12% in U. Unfortunately, none of the published CLFs/CCLFs presented here extend sufficiently deep to be able to reliably predict the number of cluster objects in CL0024+1654 at the faint end of our sample. In addition, some CLF studies (e.g. Driver et al. 1994; Wilson et al. 1997) indicate the possibility of steeper faint end slopes which would increase the fraction of cluster contaminants. In light of this, we therefore assume the generous contamination levels predicted from our fitted CLFs in the analysis which follows in this paper.

Clearly, the contamination is dominated by the cluster members. This means that the variation in contamination across the field of view is governed by their density profile. Since this increases toward the centre of the cluster and since the background number counts fall off toward the centre where the magnification is strongest (see Sect. 4.3) the observed number density of objects in the background sample is affected most by contamination at small radii. This distribution will have a strong fall-off as one moves away from the cluster centre. Fortunately, this reduces the impact of the contamination on the cumulative mass measurements (Sect. 5.3) at large radii where the strongest mass contribution comes from.

An approximate contamination profile can be obtained by assuming that the cluster mass distribution and hence the number density of galaxies is described sufficiently accurately (for this purpose at least) by an isothermal sphere (see Sect. 4.3). The radial dependence of the error on the surface mass density, κ, can thus be written

$$\sigma_\kappa(r) = \frac{k}{2nr(\beta-1)\mu^\beta(r)} \tag{4}$$

where n is the background number density in the absence of lensing, $\mu(r)$ is the magnification given by Eq. (24) and β is the number count slope (see Sect. 3.1). We have approximated the number density profile of the cluster galaxies as k/r where k is set by normalising to the contamination fractions given earlier in this section.

In all reconstructions of κ found later in this paper, we add the error given by Eq. (4) in quadrature to the sum of the other errors, including the error due to foreground galaxy contamination. The effect of contamination on the search for the U band break is discussed separately in Sect. 6.

2.5. Obscuration masks

To account for obscuration of the background sky by cluster members and foreground objects, we create a mask. Without giving consideration to obscuration, the ratio of observed objects to expected objects used later in our analysis would be biased to lower values. This is especially true of bins near the cluster centre where relatively heavy obscuration occurs due to large central cluster galaxies.

Figure 6 shows the obscuration mask produced using the SExtracted parameters of mask objects selected in Sect. 2.3. The top half shows the U band mask (grey ellipses), U band background source positions (black crosses) and the position of the annular bins used in Sects. 4.3 and 6 to bin counts radially. The lower half of Fig. 6 shows the corresponding R band mask and background sources with the grid used in Sect. 5.1 for 2D binning. Note the horizontal phase of the bins with respect to the field of view to allow placement of bin $(7,5)$ directly over the cluster centre, aligning it with the area encompassed by the critical line.

3. Mass reconstruction theory

In this section, we outline the process used for the determination of magnification from number counts. We then detail the three different methods used to transform from magnification to surface mass density.

3.1. Lens magnification: Single power-law number counts

A background population of galaxies whose integrated number counts follow the standard power-law $n(<m) \propto 10^{0.4\beta m}$ will be observed under a lens magnification factor μ to have the number count $n'(<m)$ given by (BTP, T98);

$$n' = n\mu^{\beta-1}(1+\delta_{\rm nl}) = \lambda(1+\delta_{\rm nl}). \tag{5}$$

The quantity $\delta_{\rm nl}$ accounts for perturbations in n due to non-linear clustering and we define λ as the expected number of sources in the absence of clustering. We model the fluctuation $\delta_{\rm nl}$ with a lognormal distribution and combine this with the additional uncertainty due to shot noise to give a Poisson-lognormal distribution (e.g. Coles & Jones 1991; BTP). Unlike a Gaussian distribution, the lognormal distribution accounts for non-linear clustering of the background probed by our small field of view and is positive-definite.

The Poisson-lognormal distribution can be defined as a compound distribution formed from a Gaussian distribution G of a linearised field and a Poisson distribution D as

$$P_{\rm LN}[n|\lambda(\mu)] = \int_{-\infty}^{\infty} {\rm d}\delta\, D[n|\lambda\,{\rm e}^{\delta-\sigma^2/2}]G(\delta). \tag{6}$$

Here, δ is the linear density fluctuation which relates to the non-linear fluctuation as $1+\delta_{\rm nl} = {\rm e}^{\delta-\sigma^2/2}$ with σ the linear clustering variance. Following the method of T98

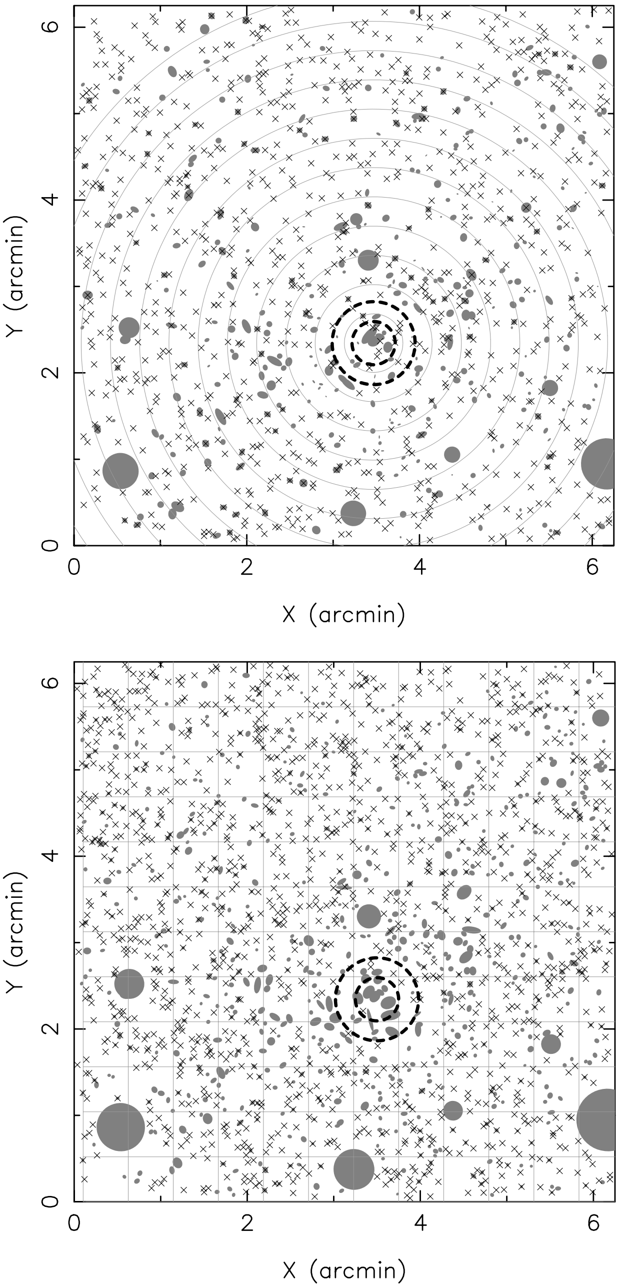

Fig. 6. *Top*: U band mask (grey ellipses) with source positions (black crosses) and annular bins used in Sects. 4.3 and 6. *Bottom*: corresponding R band mask with grid used for 2D maps in Sect. 5.1. Observed arcs lie along the outer heavy dashed circle in both plots. The inner dashed circle shows the critical line determined from the isothermal sphere model fit to the R band number counts (see Sect. 4.3).

but applied to the R band correlation function of Hudon & Lilly (1996), we calculate the non-linear clustering variance. Averaging the angular correlation function over a circular area of radius θ gives,

$$\sigma_{\rm nl}^2 = 1.5 \times 10^{-2} z^{-1.8} (\theta/1')^{-0.8}. \tag{7}$$

The linear clustering variance is calculated from the non-linear variance using $\sigma^2 = \ln(1+\sigma_{\rm nl}^2)$.

Equation (6) gives the probability distribution for the lens magnification in a given bin containing n galaxies. This directly gives the most probable magnification for that bin with its associated error taken as the width of the distribution. The integral in Eq. (6) must be evaluated numerically.

3.2. Lens magnification: Dual power-law number counts

In Sect. 6.1, we discuss evidence which suggests the presence of a break in the U band number count slope at faint magnitudes. Section 4.1 also highlights the possibility of a break in the R band counts. To account for the effect this has on the magnification calculated from number count depletion, we modify Eq. (5) to incorporate a second slope applicable beyond some break magnitude $m_{\rm b}$.

Writing the observed *differential* number counts as a dual power-law,

$$n(m) = \begin{cases} a10^{0.4\beta_1 m} & , \ m < m_{\rm b} \\ b10^{0.4\beta_2 m} & , \ m \geq m_{\rm b} \end{cases} \tag{8}$$

where the normalisation coefficients a and b are constrained by continuity, the integrated number counts up to some limiting magnitude $m_{\rm u} > m_{\rm b}$ for $\mu \geq 1$ can be expressed as

$$\begin{aligned} n'(<m_{\rm u}) \ &= \ \mu^{-1}\left[n_1(<m_{\rm b}) + \right. \\ &\left. n_2(<m_{\rm u})\mu^{\beta_2} - n_2(<m_{\rm b})\right]. \end{aligned} \tag{9}$$

Here, n_1 and n_2 denote number counts integrated up to a limiting magnitude over a constant slope of β_1 and β_2 respectively. The clustering term which features in Eq. (5) has been omitted here for clarity but is used in our analysis later.

If the limiting magnitude of observations matches the break magnitude then

$$n_2(<m_{\rm u}) = \frac{\beta_1}{\beta_2} n_1(<m_{\rm u}). \tag{10}$$

Equation (9) can thus be simplified to

$$n' = n\mu^{-1}\left[1 + \frac{\beta_1}{\beta_2}\left(\mu^{\beta_2} - 1\right)\right], \quad (\mu \geq 1) \tag{11}$$

where $n = n_1(<m_{\rm u})$ here, is the unlensed surface number count density observed, for example, at the edge of the field of view. If $\beta_1 = \beta_2$ and hence there is no break, Eq. (11) becomes Eq. (5). For the case when $\mu < 1$, Eq. (5) must be reverted to.

3.3. Local mass estimator

The simplest means of arriving at a mass estimate given a measurement of magnification is by assuming a local relationship between the convergence and shear. Such a relationship can be derived once a model is chosen to describe the mass distribution. Since magnification depends on the convergence, κ, and shear, γ, as

$$\mu = \left|(1-\kappa)^2 - \gamma^2\right|^{-1}, \tag{12}$$

this gives a directly invertible relation for μ in terms of κ and hence allows κ to be estimated.

For simplicity, we use the "parabolic estimator" suggested by the cluster simulations of van Kampen (1998) which relates γ to κ via

$$\gamma = |1-c| \sqrt{\kappa/c}. \tag{13}$$

As in T98, we adopt the value $c = 0.7$ corresponding to a profile which lies between that of a homogeneous sheet of matter ($\kappa =$ constant) and an isothermal profile ($\kappa \propto r^{-1}$, r the distance from the cluster centre). The magnification can therefore be written

$$\mathcal{P}\mu^{-1} = [(\kappa - c)(\kappa - 1/c)], \tag{14}$$

where $\mathcal{P} = \pm 1$ accounts for image parity on either side of the critical line implied by the modulus in Eq. (12). Rearranging this equation for κ gives

$$\kappa = \frac{1}{2c}\left((c^2+1) - \mathcal{S}\sqrt{(c^2+1)^2 - 4c^2(1-\mathcal{P}\mu^{-1})}\right). \tag{15}$$

The second parity $\mathcal{S}$ is due to the parabolic nature of Eq. (14) which permits a second critical line and thus higher values of κ. Since there is no evidence for the existence of a double critical line in CL0024+1654, we will adopt $\mathcal{S} = +1$ throughout this paper.

Given that the parabolic estimator requires only local κ and γ, it finds application to both radial and 2D magnification distributions in this paper.

3.4. Self-consistent axi-symmetric mass estimator

The second method which we use to estimate cluster mass is the so-called self-consistent axi-symmetric mass estimator introduced by T98. The non-local nature of this estimator allows the magnification Eq. (12) to be solved for a self-consistent κ and γ radial profile. Although the estimator is valid only for axi-symmetric mass distributions, it can be applied to data binned in any self-similar set of contours centred on the peak of the mass distribution.

In a given annular bin i, the shear can be expressed as

$$\gamma_i = |\kappa_i - \overline{\kappa}_i| \tag{16}$$

where κ_i is the convergence in the bin and $\overline{\kappa}_i$ is the convergence averaged over the area interior to and including the bin. Substituting this into Eq. (12) gives for the magnification in bin i

$$\mathcal{P}\mu_i^{-1} = (1-\overline{\kappa}_i)(1 - 2\kappa_i + \overline{\kappa}_i). \tag{17}$$

Dividing $\overline{\kappa}_i$ into two terms, one for bin i and the other, which we denote η_{i-1}, for all interior bins, so that

$$\overline{\kappa}_i = \eta_{i-1} + \frac{2}{i+1}\kappa_i \tag{18}$$

allows rearrangement of Eq. (17) to give

$$\begin{aligned}\kappa_i \;=\; & \frac{(i+1)}{4i}\big\{i + 1 - (i-1)\eta_{i-1} \\ & -\mathcal{S}[(i - 1 - (i+1)\eta_{i-1})^2 + 4i\mathcal{P}\mu_i^{-1}]^{1/2}\big\}.\end{aligned} \tag{19}$$

The parities $\mathcal{P}$ and $\mathcal{S}$ have the same function as in Sect. 3.3.

Using Eq. (19), κ is calculated iteratively. The only freedom is choice of η_0 which as Eqs. (16) and (18) show, is γ_1, the shear in the first bin. To avoid non-physical solutions, $\gamma_1^2 \geq \mathcal{P}\mu_1^{-1}$ must be enforced leaving only a sensible range of values. As T98 discuss, the overall mass and shear profile obtained with the self-consistent axi-symmetric estimator proves to have only a minor sensitivity to the choice of γ_1.

3.5. Self-consistent 2D mass estimator

The final reconstruction method we apply in this paper is that discussed by Dye & Taylor (1998). By pixellising the image into a rectangular grid of pixels, the components of the shear in any pixel n can be expressed as

$$\gamma_i^n = D_i^{mn}\kappa_m, \quad i = 1, 2 \tag{20}$$

where summation over index m is implied for all N pixels on the grid. The matrices D_1 and D_2 are simple geometrical functions of the different combinations of positions of pixels m and n (see Dye & Taylor 1998 for details).

Writing Eq. (12) in its pixellised form and substituting the expression for shear in Eq. (20) gives the vector equation

$$\mathbf{1} - 2\boldsymbol{\kappa} + \boldsymbol{\kappa}\boldsymbol{G}\boldsymbol{\kappa}^{\mathrm{t}} - \mathcal{P}\boldsymbol{\mu}^{-1} = 0 \tag{21}$$

where $\mathcal{P}$ is again the image parity from Sect. 3.3, $\boldsymbol{\mu}^{-1}$ is the N-dimensional vector of pixellised inverse magnification values, $\boldsymbol{\kappa}^{\mathrm{t}}$ is the transpose of the vector $\boldsymbol{\kappa}$ of pixellised convergence values and $\mathbf{1}$ is the vector $(1, 1, 1, ...)$. $\boldsymbol{G}$ is an $N \times N \times N$ matrix with the elements

$$G_{pqn} = \delta_{pn}\delta_{qn} - D_1^{pn}D_1^{qn} - D_2^{pn}D_2^{qn} \tag{22}$$

where δ_{ij} is the Krönecker delta, and summation occurs only over indices p and q in Eq. (21).

We solve Eq. (21) for κ using a hybrid Powell method provided by the NAG routine C05PCF.

4. Cluster model constraints from number counts

Before application of the theory presented in Sect. 3, the properties of the background population must be understood. Our initial attention is turned toward the R band population of background galaxies since this proves to be the most suitable for the application of lens magnification owing to its shallower number count slope. In this section, we use the radially binned number counts of the sample to fit an isothermal, power-law and NFW profile. We defer discussion of the U band sample properties until Sect. 6.

4.1. R band sample characteristics

The characteristics of the R band background source galaxy population must be constrained before we can apply our lensing analysis to the source counts. Specifically, the unlensed surface number density n_R and the number count slope must be determined.

T98 estimate the unlensed surface number density from deep number counts of field galaxies observed independently of their work. We opt for the alternative choice here of taking n_R from our field where the lens effect of the cluster is expected to be small. This eliminates potential biasing of the reconstructions which arise from differing completeness characteristics between the lensed field and the reference unlensed field (Gray et al. 2000). This is particularly important for the U band break search in Sect. 6.2. In an annular region centred on the cluster and bounded by the radial limits $120'' < r < 180''$, we measure $n_R = 43 \pm 2$ arcmin^{-2} in the R. This value is assumed in our subsequent analysis.

Ideally, this normalising annulus should be further away from the centre of the cluster than we have chosen. However, as we discuss in Sect. 5, the edge of our field is somewhat noisy due to the presence of some bright stars. This causes a drop in the number counts at larger radii so that normalising here would force a large over density of counts at medium radii and hence negative mass. An alternative explanation is that such an overdensity could be caused by contaminating cluster galaxies. In fact, it is most likely that both effects jointly contribute. Since our reconstructions include the uncertainty due to cluster contaminants, any bias as a result of normalising out this effect falls within our error budget. We therefore expect only a small bias to remain from the underestimation of background counts at large radii.

As far as the number count slopes are concerned, the R band slope determined by Hogg et al. (1997) over $21 < R_{\rm AB} < 25$ is $\beta_R = 0.83$, in agreement with Smail et al. (1995) who measure $\beta_R = 0.80$ over the same magnitude range. This is consistent with the slopes in the V and I from the Hubble Deep Field data of Pert et al. (1998) with $\beta_V \simeq 0.9$ and $\beta_I \simeq 0.8$ over $23 < (V,I)_{\rm AB} < 26$. However, over the fainter magnitude range $26 < (V,I)_{\rm AB} < 29$, they measure a shallower slope of $\beta_{V,I} < 0.5$ and find the trend that flattening of the number count slope is more pronounced in shorter wavelength bands. The fact that this is seen at all in the I band therefore suggests that flattening most probably also occurs in R at these faint magnitudes. This is fortified by the more recent R band counts of Metcalfe et al. (2001) from the William Herschel Deep Field, which suggest a slope of $\beta_R \simeq 0.6$ fainter than $R_{\rm AB} \simeq 26$.

Our R band observations tantalisingly extend to approximately the depth where the apparent break occurs. We compare in Sects. 4.3 and 5.3 the difference between the results obtained using the single and dual slope models. In the analysis hereafter, for the single slope model, we take $\beta_R = 0.80$ and for the dual slope model, $\beta_{R1} = 0.80$ and $\beta_{R2} = 0.5$ with a break magnitude of $R = 26$.

4.2. Magnification profiles

In the case of lens magnification, the least biased method of determining the best fit mass model is to fit depletion curves to the number count profile. In this way, the lensing signal is used in its purest form before potential biases are introduced by calculation of the κ profile.

To fit the depletion profile from a given mass model, its lens magnification must be determined. We choose to fit an isothermal sphere, a power-law mass model and a NFW profile, all of which have analytical forms for their magnification. In the case of the isothermal sphere, the mass profile is completely determined by its critical radius $r_{\rm crit}$,

$$\kappa(r) = \frac{r}{2r_{\rm crit}}, \tag{23}$$

giving a magnification of

$$\mu(r) = |1 - r_{\rm crit}/r|^{-1}. \tag{24}$$

The power-law model we choose is that of Schneider et al. (1993) which gives a smooth, non-singular surface mass density distribution with a κ profile given by

$$\kappa(x) = \kappa_0 \frac{1 + \xi\, x^2}{(1 + x^2)^{2-\xi}}. \tag{25}$$

Here κ_0 is the peak surface mass density at the centre, ξ is the power-law slope and $x = r/r_{\rm core}$ with $r_{\rm core}$ the core radius. For this distribution to remain positive definite at large radii and so that it is a declining function of radius, the valid range of slopes is $0 < \xi < 1$. At $r \gg r_{\rm core}$, this physically corresponds to a range of mass models spanning a homogeneous sheet ($\xi = 1$) through an isothermal sphere ($\xi = 0.5$) all the way up to $\kappa \propto 1/x^4$ ($\xi = 0$). The magnification resulting from such a profile is (Schneider et al. 1993)

$$\begin{aligned}\mu(x) = \; & \left[1 - \frac{\kappa_0}{(1+x^2)^{1-\xi}}\right]^{-1} \\ & \times \left[1 - \frac{\kappa_0}{(1+x^2)^{2-\xi}} \left\{1 + (2\xi - 1)\xi^2\right\}\right]^{-1}. \end{aligned} \tag{26}$$

Finally, the NFW model has a κ profile given by (Bartelmann 1996)

$$\kappa(y) = 2\kappa_s \frac{f(y)}{y^2 - 1} \tag{27}$$

where

$$f(y) = \begin{cases} 1 - \frac{2}{\sqrt{y^2-1}} \tan^{-1}\sqrt{\frac{y-1}{y+1}} & , \ (y > 1) \\ 1 - \frac{2}{\sqrt{1-y^2}} \tanh^{-1}\sqrt{\frac{1-y}{1+y}} & , \ (y < 1) \\ 0 & , \ (y = 1) \end{cases} \tag{28}$$

and $y = r/r_{\rm s}$. The scale radius, $r_{\rm s}$, and surface density normalisation, $\kappa_{\rm s}$, are free parameters of the model.

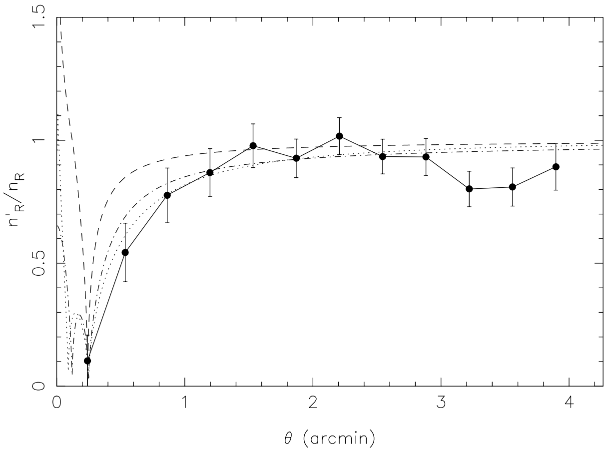

Fig. 7. Number of counts as a ratio of expected counts versus radial distance from cluster centre in the R band. Error bars account for the error in n_R and shot noise. Superimposed are the isothermal (dashes, $r_{\rm crit} = 15''$), power-law (dot-dashes, $\kappa_0 = 1.52$, $\xi = 0.61$, $r_{\rm core} = 11''$) and NFW (dots, $r_{\rm s} = 1.75'$, $\kappa_{\rm s} = 0.23$) models fit to the first 9 points.

The magnification of the NFW model comes from Jacobian determinant of the lens mapping for axisymmetric lenses (Schneider et al. 1992);

$$\mu^{-1}(y) = \left(1 - \frac{m(y)}{y^2}\right)\left[1 - \frac{\mathrm{d}}{\mathrm{d}y}\left(\frac{m(y)}{y}\right)\right] \tag{29}$$

where

$$m(y) = 2\int_0^y \mathrm{d}y'y'\kappa(y'). \tag{30}$$

4.3. Number count profile fits

Using Eq. (5) for the single slope model (and neglecting the clustering term for now) with the three forms for μ from Sect. 4.2, we perform a χ^2 fit to the observed depletion profiles. Figure 7 shows the R band radial number counts expressed as a fraction of the intrinsic background counts. The degree of obscuration by foreground objects is taken into consideration by adjusting n_R in each bin. The 1σ error bars plotted account for the uncertainty in n_R and shot-noise.

Superimposed on the observed R band number counts in Fig. 7 are the isothermal, power-law and NFW profiles obtained from fitting to the first 9 data points. We discuss in Sect. 5.1 that the outer profile is affected by noisy features at the edge of the field of view. The final model fits therefore omit the last 3 points although we also fit to all 12 points to investigate the variation in fitted parameters.

For the isothermal profile, a best fit critical radius of $r_{\rm crit} = 15''\pm1''$ is obtained using either the first 9 points or all 12 points. Note that this is somewhat smaller than the estimate of $r_{\rm crit} = 25''$ in the R band from R01. This discrepancy arises partly from the different object selection and extraction criteria used by R01, detailed in Sect. 2, and also from our different radial bin width. The error of $\pm1''$ we quote here is solely the error from the χ^2 fit which does not include any uncertainty to allow for the choice of binning. Variation in bin width and also the radius attributed to a given bin adds further error. In Fig. 7, the radial position of a given bin is taken as the radius which divides that bin into two equal areas. Since the isothermal fit is dominated by the radius of the first data point, adopting different binning strategies affects the fitted value of $r_{\rm crit}$ substantially. Measuring the variation in fitted values of $r_{\rm crit}$ with different binnings, we find that a further error of $\pm10''$ should be included to give an overall fit of $r_{\rm crit} = 15'' \pm 10''$.

The observed radius of the large arcs, $r_{\rm arc} = 30''$, is also somewhat larger than our fitted critical radius. One explanation for this would be that the background population we select lies at a lower redshift on average than the lensed background galaxy forming the arc at $z = 1.675$ (B00). In fact, knowing the amount of mass contained within the arcs (see Sect. 5.3), one finds that a critical radius of $r_{\rm crit} = 15'' \pm 10''$ corresponds to a background population with a mean redshift lying within the range $0.40 < z_{\rm mean} < 0.82$ (EdS or $\Omega = 0.3$, $\Lambda = 0.7$). Note that although this range appears to permit only quite low mean redshifts, it depends sensitively on the confidence interval. For example, expanding the interval from 68% quoted above to merely 80% results in a range $0.40 < z_{\rm mean} < 1.19$. Clearly, the large error on $r_{\rm crit}$ prevents an accurate measurement of $z_{\rm mean}$.

However, considering the redshift survey of Cohen et al. (2000) in the Hubble Deep Field North region, this indicates a median redshift of $z_{\rm median} = 0.79^{+0.30}_{-0.31}$ in their deepest bin at $R_{\rm AB} \simeq 24$. Extrapolating their $z_{\rm median}$ versus magnitude plot by a further 1.5 mags to coincide with our 3σ detection limit and weighting by the expected number counts over this interval, one obtains an approximate mean redshift expected for our background R sample of $z_{\rm mean} \sim 1.2$. Therefore, although our lens-inferred measurement of $z_{\rm mean}$ is a little low, it is not significantly inconsistent.

The choice of bin width of $20''$ means that our ability to constrain the small scale core radius in the power-law profile is very limited. In fitting to the power-law, we therefore hold $r_{\rm core} = 11''$ determined by the shear study of CL0024+1654 by TKD which has superior resolution in the centre of the cluster. Fitting the remaining two parameters to the first 9 points then yields $\kappa_0 = 1.52 \pm 0.20$ and $\xi = 0.61 \pm 0.11$ with 1σ errors accounting for the fit and binning variation. This compares to $\kappa_0 = 1.42 \pm 0.21$ and $\xi = 0.67 \pm 0.11$ obtained when the remaining 3 points are included.

Finally, fitting the NFW model to the first 9 points yields the parameters $r_{\rm s} = 1.75' \pm 1.02'$ and $\kappa_{\rm s} = 0.23 \pm 0.08$. Including all 12 points, these become $r_{\rm s} = 2.50' \pm 1.32'$ and $\kappa_{\rm s} = 0.19 \pm 0.08$. The large errors here reflect a strong degeneracy between $\kappa_{\rm s}$ and $r_{\rm s}$.

Although close to isothermal with a slope of $\xi = 0.61$, the power-law model provides a better fit to the number counts than the isothermal sphere. The NFW and power-law models are clearly very similar however the reduced χ^2

of 0.41 ± 0.53 from the NFW model (assuming Gaussian statistics to obtain the error) quantifies the fact that it is a better fit to the data than the PL model with a reduced χ^2 of 0.62 ± 0.53 including the first nine bins. For comparison, the isothermal sphere model fits to the data with a reduced χ^2 of 1.33 ± 0.50. This agrees with the findings of TKD who concluded that although the NFW profile predicts too much mass within the inner arc region, there is little to distinguish this from a power-law profile at larger radii. In fact, with all 12 bins in the fit, the PL model fares best with a reduced χ^2 of 1.08 ± 0.45 compared with that of the NFW model of 1.24 ± 0.45.

Our magnification profile fits prove to be consistent with fits to shear-derived mass profiles from other work. TKD find that the mass profile of CL0024+1654 is best described by a power-law model with $\xi = 0.57 \pm 0.02$ and a central surface mass density of $\Sigma_0 = 7900 \pm 100\ h\,M_\odot\ \mathrm{pc}^{-2}$. We can compare this central surface mass density with our estimate of κ_0 by integrating our fitted power-law model for κ over the disk enclosed by the observed arcs. Comparing this with the real projected mass contained within this area from Sect. 5.3 allows the normalisation of the model to be calculated. This requires a central surface mass density of $\Sigma_0 = 9000 \pm 1800\,h\ M_\odot\ \mathrm{pc}^{-2}$, slightly higher than the TKD estimate but consistent given the error budget.

Similarly, B00 find that their azimuthally averaged mass profile for CL0024+1654 is close to the NFW prediction for massive clusters with an overdensity of $\delta_\mathrm{c} \simeq 8000$ and $r_\mathrm{s} \simeq 400\,h^{-1}\,\mathrm{kpc}$ (NFW, Ghigna et al. 1998). Using the fact that $\delta_\mathrm{c} = \kappa_\mathrm{s}\Sigma_\mathrm{CR}/(r_\mathrm{s}\,\rho_\mathrm{crit})$ (Bartelmann 1996) where Σ_CR is the critical lens surface mass density (see for example Blandford & Narayan 1992) and ρ_crit is the critical density of the Universe, this converts to $\kappa_\mathrm{s} \simeq 0.2$ with a scale radius $r_\mathrm{s} \simeq 2'$. The findings of this paper are therefore in good agreement with the NFW expectation.

Finally, we have also applied the dual slope model to fit the three profile forms with magnification calculated using Eq. (11). We find that this gives fitted model parameters within a few percent of those presented above. As expected, this negligible difference indicates that the lensing signal in the R band is dominated by galaxies in the $R < 26$ mag range where the steeper slope applies, despite flux magnification of objects by CL0024+1654.

5. Cluster mass reconstructions

In this section, we present the results of the 2D and radial mass reconstructions obtained using the R band background galaxy sample.

5.1. 2D mass maps

Using the 12×12 grid of bins shown in Fig. 6 and the associated R band obscuration mask, source numbers were binned across the field of view and used to calculate magnifications using Eq. (6). Applying both the local estimator and the self-consistent reconstruction method assuming single slope counts, we derive the mass maps shown in Fig. 8. The top half of this figure shows the locally estimated κ for comparison with the lower half showing the self-consistent mass distribution.

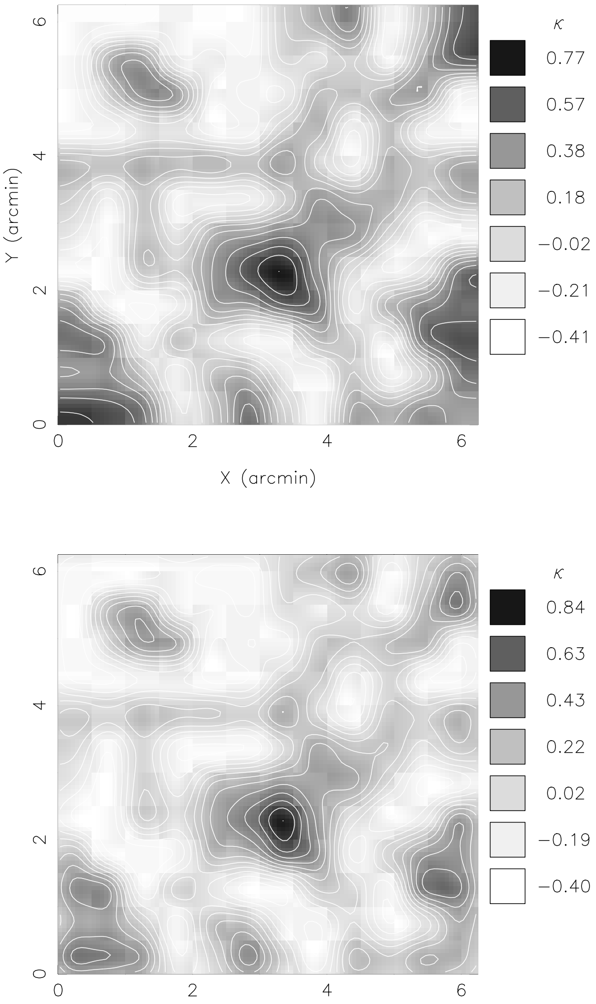

Fig. 8. Mass reconstruction from the R band data. *Top*: estimated κ from parabolic estimator. *Bottom*: iterated self-consistent κ. Contours in both plots are separated by intervals of $\delta\kappa = 0.1$. North is up, East is left.

Both maps exhibit a very similar mass structure demonstrating that the local estimator works well. The peak of the distribution in the self-consistent map is slightly higher than in the estimated map and is more distinct from the surrounding mass fluctuations. This is especially true at the edge of the field where noisy features in the estimated map have been suppressed by the non-local solution provided by the self-consistent method. In particular, the features seen in the lower left and lower right corners due to a large degree of obscuration by the two brightest stars in the field (which is difficult to properly account for) have been suppressed significantly. In addition, the large dip seen in the top left corner caused by an excessive number of background sources has been slightly reduced.

The error map calculated from the width of the probability distribution in Eq. (6) indicates that the significance of the peak in the self-consistent map is 6σ. If we include the extra uncertainty due to contamination by cluster objects at the predicted level of 19% as well as the error in the unlensed surface number density, this significance drops to 4σ. Note that the peaks in both plots appear lower than the peak value implied by the radial analyses. This is a direct consequence of the relatively low resolution of the 12×12 grid of bins which has averaged over the central cluster region and effectively smoothed out the peak. This same reason describes the apparent discrepancy with the shear-derived mass maps of TKD and B00, both of which cover a much smaller field of view ($\sim 1.5' \times 1.5'$) and both of which imply a peak of $\kappa \simeq 1.3$.

This resolution effect in the maps does not affect the shape of the radial mass profiles because it occurs on a scale smaller than the radial bin size. Section 5.2 verifies this since the profiles obtained agree with the power-law model which predicts a central surface mass density of $\kappa \simeq 1.4$. Furthermore, the local estimator agrees with the non-local estimator which would certainly not be the case if the bin resolution caused an effective smoothing of the profile. The cumulative mass measurements derived from the profiles are also therefore not affected.

The topology of the structure seen in the mass maps is very similar to the distribution of cluster light (Fig. 3) and the cluster galaxy number density (Fig. 2). In the mass map, we find a relatively compact core with extensions toward the north-west and south-west (toward the top-right and bottom-right in Fig. 8 respectively). In comparing these extensions with the light and number density distributions, it is noticeable that the light traces the north-west extension more than the south-west, whereas the number density traces the south-west extension more than the north-west. The explanation is that in the north-west, there are fewer galaxies, forming an almost distinct sub-clump, but they are relatively bright. In contrast, the south-west extension harbours a higher number of fainter cluster members.

Comparison of our mass map with the X-ray map of Soucail et al. (2000) again shows very similar structure. The X-ray contours show an elongation along the south-west direction while a separate peak of X-ray emission is seen toward the north-west, coinciding with the sub-clump of large cluster galaxies noted above. Soucail et al. suggest that the emission originates from one of two possible sources. The closest to the centre of the emission is a large cluster galaxy lying at a redshift of $z = 0.4017$ while the other is a foreground star-forming galaxy at $z = 0.2132$. Given our detection of mass and the concentration of large cluster galaxies in this region, it seems plausible to explain at least part of the X-ray emission as being due to cluster gas. The fact that the X-ray map shows a distinct peak suggests that this is actually a separate mass clump rather than an extension. The shear map of TKD shows no evidence of there being such a sub-clump although B00's map suggests that extra mass lies in this vicinity. Unfortunately, neither of these shear maps cover a wide enough field of view for this to be properly verified.

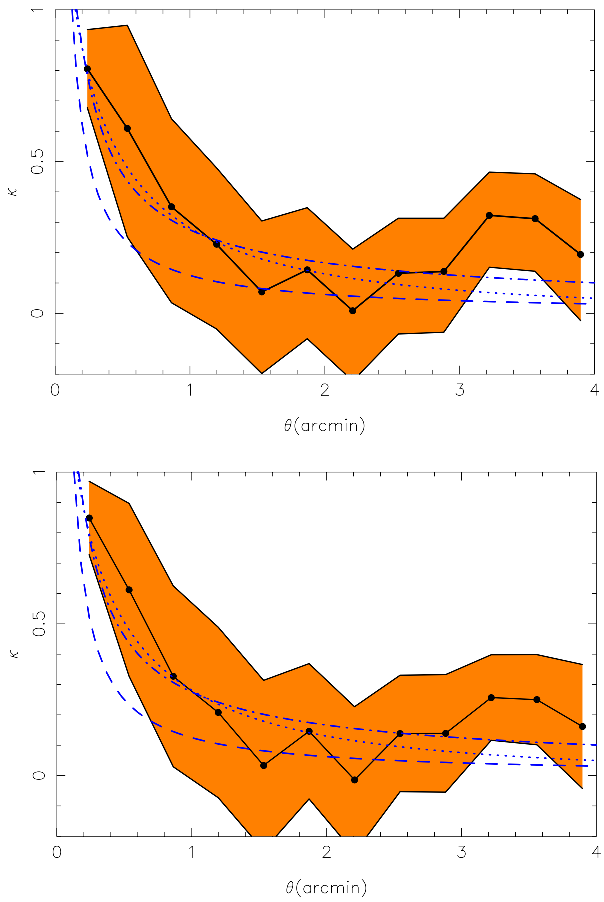

Fig. 9. *Top*: locally estimated radial mass profile for R band sources binned using annuli shown in Fig. 6. The shaded region shows the 1σ uncertainty which allows for shot noise, source clustering, uncertainty in background count normalisation and 19% cluster contamination. *Bottom*: axi-symmetric solution for the R band. Both plots show the isothermal (dashes), power-law (dot-dashes) and NFW (dots) models fitted to the first 9 data points (see Sect. 4.3).

5.2. Radial mass profiles

In Fig. 9 we show the radial mass profile calculated for the R band sources using both the local estimator and the axi-symmetric method assuming the single number count slope model. For calculation of the axi-symmetric profile, the value of the shear in the first bin is set to $\gamma_1 = 0.25$ (see Sect. 3.4). The shaded regions in both plots show the 1σ uncertainty accounting for shot noise, source clustering, uncertainty in background count normalisation and 19% cluster member contamination. Similar to the 2D mass distribution, we find that the last 3 data points in the axi-symmetric solution are slightly suppressed compared to the local estimator.

The fitted profiles of Sect. 4.3 plotted in Fig. 9 again show that the power-law and NFW models give a better fit to the results. Both profiles exhibit an excess of mass

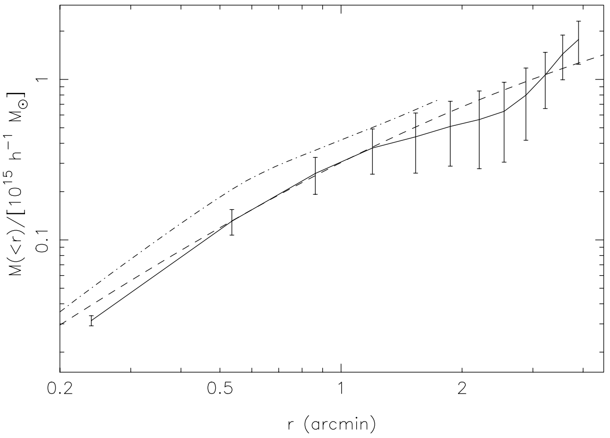

Fig. 10. Cumulative projected mass calculated by normalising to the amount of mass enclosed within the circle traced by the observed arcs. Also plotted is the NFW model of Sect. 4.3 (dashes) and the B band results of van Kampen (1998) (dot-dashes).

at $3'' < r < 4''$. This is attributed to the noisy features seen in the 2D mass plots at the edge of the field, and just pushes the measured mass at this radius to a value inconsistent with the NFW and power-law fit.

5.3. Cumulative mass profile

To convert from κ to real projected mass, we normalise to the amount of mass contained in the disk traced by the observed arcs. Since the enclosed mass can be calculated to a high accuracy, normalising in this way provides a much more reliable scaling than using a mean redshift estimated for the background population. Using B00's measurement of the redshift of the arcs at $z = 1.657$, the mass within a radius of $r_{\rm arc} = 30''$ from the centre of the cluster can be calculated to be $1.19 \times 10^{14}\ h^{-1} M_\odot$ for an Einstein de Sitter (EdS) Universe. The cosmological dependence of this result is weak to the extent that for an $\Omega = 0.3$, $\Lambda = 0.7$ cosmology, this enclosed mass increases by only 5%. This scaling applies generally hence all aperture masses quoted hereafter assume an EdS cosmology.

Scaling our radial κ profile with this normalisation, we sum the mass in each bin to produce the cumulative projected mass profile in Fig. 10. Out to a radius of $2.9'$ ($0.54\,h^{-1}$ Mpc for EdS), we measure a projected mass of $(8.1 \pm 3.2) \times 10^{14}\ h^{-1} M_\odot$. The 1σ error here again includes shot noise, source clustering, uncertainty in background count normalisation and contamination from cluster members at the 19% level. If we apply the dual slope model, we find a mass of $(8.2 \pm 3.2) \times 10^{14}\ h^{-1} M_\odot$, re-iterating the statement made in Sect. 4.3 that the lensing signal in the R band is dominated by galaxies in the $R < 26$ mag range where the slope $\beta_R = 0.80$ applies.

Approximating the integrated NFW profile, the projected mass within a radius R scales as $M(<R) = 2.9 \times 10^{14}\ (R/1')^{1.3-0.5\,\lg(R/1')}\ h^{-1} M_\odot$. With this scaling relation for the cumulative mass, we can readily compare our results with other authors. Considering existing lensing measurements for the moment, the measurement by B00 of the mass contained within the arcs obviously agrees with our estimation by default since this is essentially the mass we normalise to. Using the redshift of the arc from B00, TKD's estimate of the cluster mass contained within a radius of $107\,h^{-1}$ kpc is $(1.553 \pm 0.002) \times 10^{14}\ h^{-1} M_\odot$. At this radius, our NFW estimate for the enclosed mass is $(1.3 \pm 0.3) \times 10^{14}\ h^{-1} M_\odot$. Extending to slightly larger radii, the magnification analysis of van Kampen (1998) finds a projected mass of $(6.7 \pm 2.0) \times 10^{14}\ h^{-1} M_\odot$ within $300\,h^{-1}$ kpc compared to our NFW mass of $(5.0 \pm 1.7) \times 10^{14}\ h^{-1} M_\odot$. On even larger scales, the weak shear study of Bonnet et al. (1994) measures a mass of $(1.6 \pm 0.4) \times 10^{15}\ h^{-1} M_\odot$ within $R = 1.5\,h^{-1}$ Mpc compared with our prediction of $(1.7 \pm 0.7) \times 10^{15}\ h^{-1} M_\odot$.

In terms of mass-to-light, using the surface flux density of cluster galaxies plotted in Fig. 3, we find a ratio of $M/L_B = 330 \pm 30$ (total mass/total light in B) within a radius of $0.5'$. This error accounts for uncertainty in the photometric zero point but does not reflect the fact that this is effectively an upper limit as a result of potentially missing cluster galaxies in our selection process (Sect. 2.3). Again, since our mass within this radius agrees with that of B00, we find an almost identical result to B00's result of $M/L_B = 320 \pm 30$. On a slightly larger scale, we measure $M/L_B = 480 \pm 180$ within $1'$ where now the error includes additional uncertainty from the mass error. Finally, out to $2.9'$, we find $M/L_B = 470 \pm 190$. These latter two measurements are consistent with a mass-to-light ratio which increases on larger scales although a scale-independent ratio, as found by Kochanski et al. (1996), remains plausible given the errors.

In Fig. 10, we also plot the only other magnification based cumulative mass profile of CL0024+1654 which exists to date; that of van Kampen (1998). This was derived from the B band observations of the cluster by Fort et al. (1997). We choose the B band data in favour of the I which suffered contamination from an unusual speckle beam pattern coming from stray light in the telescope optics (Fort 2001, private communication). This resulted in an over-exaggerated zone of depletion in the I band radial number counts. Notice that van Kampen's B band mass profile agrees very well with our data points in terms of its shape but that its normalisation is higher by ~30%.

Turning to alternative methods for the determination of cluster mass, Czoske et al. (1999) using galaxy dynamics from 227 spectra measure the 3D mass of CL0024+1654 to be $(1.4 \pm 0.3) \times 10^{14}\ h^{-1} M_\odot$ within a radius of $500\,h^{-1}$ kpc. Converting this to a projected mass using the isothermal sphere model they assume, yields a value of $(2.2 \pm 0.5) \times 10^{14}\ h^{-1} M_\odot$. This agrees with the X-ray temperature measurements by Soucail et al. (2000) who measure a projected mass of $2.3^{+2.0}_{-0.8} \times 10^{14}\ h^{-1} M_\odot$ within the same radius. Our scaling relation gives a projected mass enclosed by this radius of $(8.0 \pm 3.1) \times 10^{14}\ h^{-1} M_\odot$. It should be noted that the later redshift measurements of Czoske et al. (2001a) indicate that CL0024+1654 is a perturbed system. This implies that mass measurements of the cluster which assume dynamical equilibrium are probably not reliable. We discuss the significance of this in Sect. 7.

6. The U band galaxy population

The role of the U band population thus far has been to assist in the selection of R band background galaxies through colour cuts. In this section, we test the feasibility of using the U band for detection of lens magnification through number counts. We wish to re-examine the claim made by R01 that the number count slope of the background field galaxy sample becomes flatter than the lens invariant slope, $\beta = 1$, at faint magnitudes.

6.1. The U band number count slope

Current evidence regarding the notion of a break in the U band field galaxy number count slope at faint magnitudes is tenuous. At magnitudes brighter than $U_{\rm AB} \simeq 25.5$, there is good convergence. All studies agree that at these brighter magnitudes, the number count slope is relatively steep. Pozzetti et al. (1998), in analysing the Hubble Deep Field North (HDF-North), find that for $23 < U_{\rm AB} < 25.5$, $\beta_U = 1.00$ whereas Hogg et al. (1997) conclude that $\beta_U = 1.17$ for $U_{\rm AB} < 25.5$ from ground based observations.

At fainter magnitudes, Pozzetti et al. (1998) measure a much flatter slope of $\beta_U = 0.34$ at $U_{\rm AB} = 25.8$ from the HDF-North. Similarly, at the same magnitude, Metcalfe et al. (2001), using a combination of the ground based William Herschel Deep Field and the HDF-North and HDF-South, report a slope of $\beta_U = 0.38$. This appears to contrast with the results of Volonteri et al. (2000) who measure a slope of $\beta_U = 1$ up to $U_{\rm AB} \simeq 26.5$ with the HDF-South.

The depth of our observations in the U band extend to approximately the suggested U band break magnitude, which at first sight, appears to extinguish any hopes of pushing the search beyond current limits. However, we are in a fortuitous position for two reasons. The first is that our analysis merely rests upon the *relative* depletion of galaxy numbers. As Gray et al. (2000) demonstrate, this means that provided the completeness characteristics of the unlensed reference number counts are the same as the lensed field, the completeness function drops out of Eq. (5). Our reference counts are taken from the edges of our cluster field so by definition have the same completeness characteristics. In the same way that the completeness function drops out of Eq. (5), it also drops out of Eqs. (11) and (31). This is an important result and means that our break search is not affected by incompleteness. We therefore need not concern ourselves with completeness corrections such as those applied to existing traditional number count measurements which may cause a potentially large uncertainty at faint magnitudes.

Our second fortuity lies in the fact that our observations are of a cluster-lensed field, enabling us to exploit the effect of flux magnification on our background sample. Taking the NFW model fit from Sect. 4.3, this predicts that within a disk of diameter $0.8'$ centred on the cluster, lens magnification by CL0024+1654 pushes the effective limiting magnitude of our observations by $\Delta m \geq 2.5$. Within a disk of diameter $2'$, this becomes $\Delta m \geq 0.8$. We are therefore able to use our dataset to search for a break in the U band number counts some way beyond the physical limiting magnitude of our data.

Note that this does not contradict the discussion earlier that allowing for a dual slope in the R band lensing analysis causes little difference to the results obtained. It is true that both the U and R band samples extend to approximately where the break magnitude is thought to lie and it is also true that lens magnification acts on both samples equally to increase the effective depth of each. In the case of the R band sample however, the determination of mass depends on the *joint* contribution from both the steep and shallow number count slopes. In the search for the U band break as we discuss in detail below, these contributions are considered *separately* so that the more numerous galaxies in the steep slope region do not dominate those beyond the break magnitude. In addition to this effect, the expected U band change of slope of $\beta_U \simeq 1 \rightarrow 0.3$ is more severe than the expected R band change of $\beta_U \simeq 0.8 \rightarrow 0.5$. This makes detection of any faint slope depletion easier and hence further increases the confidence limits we can place on our search results.

6.2. Testing for a U band break

We use two number count models to search for a break magnitude. The first is a modification of the single slope number count scenario to allow the slope to smoothly flatten off beyond the break magnitude. The second uses the dual slope model of Sect. 3.2, allowing the faint slope to vary.

6.2.1. Model 1

The first model generalises the single slope number count model to include an arbitrary cut-off at U_0;

$$n'_U = n_U \mu^{\beta_U - 1} \left[\frac{1 + 10^{0.4\beta_U \Delta U}}{1 + \mu^{\beta_U} 10^{0.4\beta_U \Delta U}} \right], \tag{31}$$

where $\Delta U = U_{\rm lim} - U_0$ and $U_{\rm lim}$ is the limiting magnitude of the observations, $U_{\rm lim} = 25.7$. Well below the break scale, $U_0 \ll U_{\rm lim}$, or for weak lensing $\mu \approx 1$, this reduces to the usual scaling for lensing of a single slope number count distribution in Eq. (5). Above the break scale, Eq. (31) tends toward the scaling $n' = n\mu^{-1}$, for a completely flat number count distribution.

We take the best fit NFW profile determined from the R band data to provide the magnification in Eq. (31). The free parameters of the model are therefore the break scale, U_0, and β_U which we fit by maximising the following likelihood function:

$$\mathcal{L} \propto \left\langle \prod_i \exp\left(\frac{-[n'_{U,i} - p_{U,i}(U_0, \beta_U) - c_i]^2}{n_{U,i}} \right) \right\rangle_{\mathrm{c}} . \qquad (32)$$

Here, $n'_{U,i}$ is the number of U band objects observed in bin i, $n_{U,i}$ is the number expected in the absence of lensing and $p_{U,i}$ is the number predicted by the NFW profile fitted to the R band data. The product acts over all annuli. Uncertainty due to cluster and foreground galaxy contamination is incorporated through the quantity c_i. The foreground galaxy component of c_i is set at 3% of $n_{U,i}$ for each bin, in accordance with the contamination fraction discussed in Sect. 2.4.1. The cluster component of c_i varies with choice of CLF. We therefore average over different realisations of the CLF, weighting by the probability distribution obtained from fitting to our known U band cluster counts (see Sect. 2.4.2). As in Sect. 5, the radial variation of cluster number count density is taken to be k/r where k is set by normalising to the contamination determined for each CLF realisation.

The top half of Fig. 11 shows the χ^2 contours obtained from the likelihood distribution of Eq. (32). With a 95% confidence, our data rules out a complete flattening of the U band counts with a break magnitude brighter than $U_{\mathrm{AB}} = 27.3$. Furthermore, we measure the U band slope as $\beta_U = 1.07 \pm 0.06$. This is very close to the lensing invariant slope $\beta = 1$ which causes the increase in surface number density due to flux magnification to exactly cancel the dilution caused by magnification of their inter-spacing. The claim made in Sect. 4 that the U band population is unsuitable for the detection of magnification from number counts is thus substantiated.

Figure 12 shows the U band radial number count profile observed. In this plot, the model fits determined in Sect. 4.3 are used to predict counts assuming $\beta_U = 1.07$. The predictions and measurements are clearly consistent with each other. There is little distinction between any of the predicted profiles due to the near lensing invariant slope. This serves to demonstrate the insignificant depletion signal imposed on the number counts in the U band.

6.2.2. Model 2

The second method we use to search for a break assumes the dual number count slope model described in Sect. 3.2. For the purpose of our analysis in this section, we hold the bright slope at the value determined previously, $\beta_{U1} = 1.07$. The faint slope β_{U2} and the break magnitude are allowed to vary in our minimisation.

The lower half of Fig. 11 shows the results of this minimisation. Slightly more relaxed than the previous result, the data rule out a complete flattening ($\beta_{U2} = 0$) brighter than $U_{\mathrm{AB}} = 26.6$ at a confidence level of 95% . As the faint slope is allowed to steepen, this limit slips to brighter magnitudes as a result of the degeneracy between both parameters (Pozzetti at al. 1998). However,

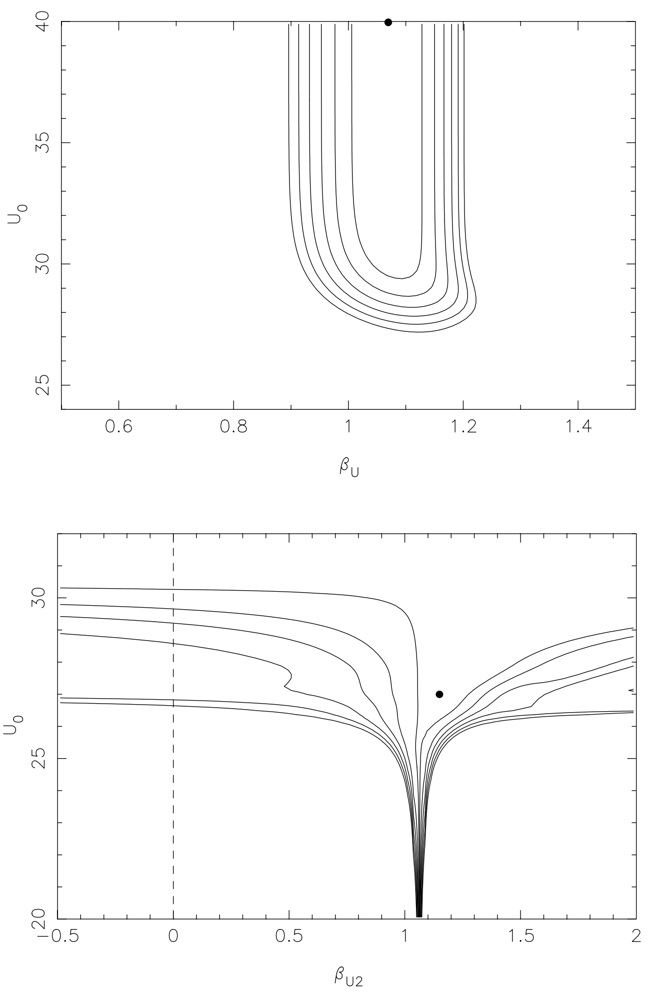

Fig. 11. *Top*: χ^2 distribution of the U band number count slope β_U and the break scale U_0 assuming the number counts flatten off completely at faint magnitudes. *Bottom*: χ^2 distribution of the faint number count slope β_{U2} and the break scale holding the bright slope at $\beta_{U1} = 1.07$. All contours are separated by $\Delta\chi^2 = 1$.

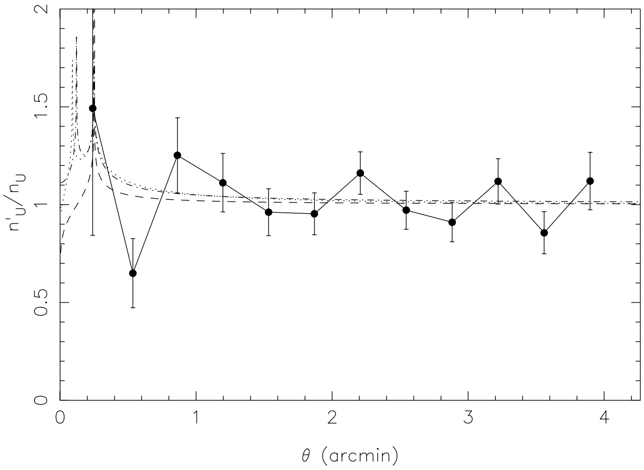

Fig. 12. Radial number count profile in the U band. Superimposed are the best fit isothermal (dashed line), power-law (dot-dashed line) and NFW (dotted line) models using the number count slope $\beta_U = 1.07$. Error bars account for the error in n_U and shot noise.

a slope of $\beta_{U2} = 0.4$, the value reported by Pozzetti et al. (1998) and Metcalfe et al. (2001) as being applicable fainter than $U_{\mathrm{AB}} \simeq 25.5 \rightarrow 26$, can be ruled out to $U_{\mathrm{AB}} < 26.4$ with 95% confidence. Pushing this limit further still, the contours in Fig. 11 show that a slope even as steep as $\beta_{U2} = 0.8$ can be ruled out with 95% confidence to $U_{\mathrm{AB}} < 26.0$. Finally, at $\beta_{U2} = \beta_{U1}$, where the degeneracy between the faint and steep slope is 100%, the break magnitude cannot be constrained at all.

We note that these results are also inconsistent with the findings of R01 who suggest a *combined* slope (i.e. the effective single slope causing the same level of depletion as a dual-slope model, steeper than the faint end slope) of $\beta \simeq 0.5$.

7. Summary and discussion

From U and R band observations of the cluster CL0024+1654, we have selected a background sample of galaxies in both bands using colour information. The cluster member contaminants identified by matching with the Czoske et al. (2001a) redshift survey of the field have been discarded from the U band. We have computed the cluster luminosity function of CL0024+1654 in both bands. This has been used in conjunction with the U and R field galaxy luminosity function from the CNOC2 survey (Lin et al. 1999) to estimate foreground and cluster contamination of our background samples. In the R band, we estimate a total contamination of 21% in contrast to a smaller 12% in the U, where the cluster component is calculated from our own fitted CLF.

The shallower number count slope observed in the R band sample makes this suitable for an investigation into the lens magnification induced depletion of background number counts. Depletion in this sample has indeed been detected and used to measure the radial and two dimensional distribution of mass in the cluster. Out to a radius of $0.54\,h^{-1}$ Mpc, we measure a total projected mass of $(8.1 \pm 3.2) \times 10^{14}\ h^{-1}\,M_{\odot}$ where the 1σ error includes shot noise, source clustering, uncertainty in background count normalisation and contamination from cluster and foreground galaxies. We find that this result increases by merely ~2% when we allow for a flattening in the R band number count slope at $R_{\mathrm{AB}} = 26$. Claims of such a change in slope have been reported by several authors (e.g. Pozzetti et al. 1998; Metcalfe et al. 2001), however allowing for it in our depletion analysis makes little difference due to the lensing signal being dominated by galaxies brighter than the break.

Converting the R band flux from selected cluster galaxies to the B band, we find a mass-to-light ratio of $M/L_B = 330 \pm 30$ inside an aperture of radius $0.5'$ centred on the cluster. Since our selection process will have inevitably missed cluster galaxies, neglecting their contribution to the total luminosity, this is effectively an upper limit. On a slightly larger scale, we measure $M/L_B = 480 \pm 180$ within $1'$ and also $M/L_B = 470 \pm 190$ within $2.9'$ ($0.54\,h^{-1}$ Mpc). These latter two measurements are consistent with a mass-to-light ratio which increases on larger scales although a scale-independent ratio remains plausible given the errors.

We have compared the observed radial depletion with that expected from an isothermal, power-law and NFW mass profile by fitting the predicted magnification of each. The NFW model provides the best fit to our data however there is little distinction between this and the power-law model. This agrees with the findings of Tyson et al. (1998) as does the mass of $1.3 \times 10^{14}\ h^{-1}\,M_{\odot}$ we measure within the disk described by the large arcs compared to their estimate of $(1.553 \pm 0.002) \times 10^{14}\ h^{-1}\,M_{\odot}$. Approximating the fitted cumulative NFW model, the projected mass contained within a radius R scales approximately as $M(<R) = 2.9 \times 10^{14} (R/1')^{1.3-0.5\,\lg(R/1')}\,h^{-1} M_{\odot}$. Together with the cluster galaxy light and number density distribution, our 2D mass maps suggest the existence of a separate sub-clump of mass just north-west of the cluster centre. This claim is strengthened by the detection of distinct X-ray emission in this area (Soucail et al. 2000) as well as the suggestion of extra mass from the shear mass map of Broadhurst et al. (2000).

In fitting the number counts to the isothermal sphere mass model, we find that the fitted critical radius is smaller (although not significantly given the error) than the radius of the circle traced by the observed large arcs. This might be due to the fact that our selected background population of sources lies at a lower mean redshift than the lensed galaxy forming the arc at $z = 1.675$ (Broadhurst et al. 2000). The mean background source redshift in an 80% confidence interval is inferred to be within $0.40 < z_{\mathrm{mean}} < 1.19$. The depletion analysis of CL0024+1654 by Fort et al. (1997) in the B band finds a relatively wide depletion profile (see Sect. 5.3 regarding contamination of their I band data). Simultaneously fitting to a maximum of five isothermal sphere models, they find that a combination of various background galaxy populations is required to explain the wide zone of depletion. In B, this results in the mean background source redshifts ranging over $z = 0.9^{+0.1}_{-0.1}$ to $z = 3.0^{+1.8}_{-0.5}$ with 42% of sources lying at $z = 0.9$. This is a little surprising given that we find an adequate fit to our observed depletion profile assuming the existence of only one critical line. The discrepancy would perhaps be at least partially resolved by fitting the Fort et al. data to an NFW profile since this accommodates a larger zone of depletion compared to the isothermal sphere model.

Comparison of our results or indeed any of the existing lensing results with those measured using cluster galaxy dynamics or X-ray temperatures shows a large discrepancy. We predict approximately 3.5 times as much projected mass as the X-ray and dynamical measurements imply. Soucail et al. (2000) discuss that one explanation for this discrepancy may come from the inability to correctly measure lens shear combined with a lack of accurate knowledge of the background source redshift distribution. While this bears some truth in general, it is not the case here. The determination of the arc redshift by Broadhurst et al. (2000) makes the measurement of projected mass contained within the arc radius a robust one; this is a result which does not depend on the detection of shear through weak lensing and also knowing the redshift of the arced galaxy breaks the source redshift degeneracy. The projected mass contained within the arc radius according to the X-ray measurements of Soucail et al. is $(0.5 \pm 0.3) \times 10^{14}\ h^{-1}\ M_{\odot}$. This is still a factor of nearly three times smaller than the arc predicted mass.

An alternative scenario which provides a more satisfying answer to the evidence gained thus far is alignment of additional foreground and/or background mass along the line of sight to CL0024+1654. The Czoske et al. (2001a) redshift survey identifies a group of galaxies lying just in front of the cluster as well as a pair of groups lying behind it. During the course of preparing this paper, new evidence emerged regarding the perturbed galaxy dynamics of CL0024+1654. Comparing numerical simulations with their redshift measurements, Czoske et al. (2001b) conclude that the cluster could in fact be the result of a high speed collision of two smaller clusters along the line of sight. This would certainly explain why lensing observes a factor of three times as much mass. It also explains why early measurements of velocity dispersion were very large (see Dressler & Gunn 1992 and references therein); these were based on ~10 times fewer redshifts and hence failed to properly resolve the cluster's true dynamical state.

Finally, the U band selected background sample indicates a near-lensing-invariant slope of $\beta = 1.07 \pm 0.06$ and hence does not exhibit any noticeable sign of depletion. We have used the fact that lens magnification of our U band sample allows us to search deeper than its physical limiting magnitudes thus facilitating the search for a change of slope in the U band number counts at faint magnitudes. Up to $U_{\rm AB} \leq 26.6$, we can rule out a complete flattening to 95% confidence. Furthermore, we can rule out the existence of a change of slope of $\beta = 1 \rightarrow 0.4$ reported by Pozzetti et al. (1998) and Metcalfe et al. (2001) with a confidence of 95% up to $U_{\rm AB} \leq 26.4$.

Our findings also contradict the results of R01 who claim to have measured U band depletion and hence slope flattening. Although we started with the same observations as R01, we applied more stringent criteria to the object extraction and carried out a thorough U band break analysis which allowed for contamination by cluster and foreground galaxies. It is intriguing that the HDF-South U band number counts reported by Volonteri et al. (2000) also support our result. They too find no evidence of flattening in the U band counts up to $U_{\rm AB} \simeq 26.5$. This will most likely remain an unresolved issue until deeper observations, particularly in a cluster environment where lens magnification provides natural assistance, are obtained.

Acknowledgements. SD thanks PPARC for financial support as a PDRA. ANT is a PPARC Advanced Fellow. Thanks to Chris Pearson for helpful input from his source number count models. Finally, we thank Ian Smail as referee of this paper for his constructive comments. This work was supported in part by The Icelandic Research Council and The Research Fund of the University of Iceland. The Nordic Optical Telescope is operated on the island of La Palma jointly by Denmark, Finland, Iceland, Norway, and Sweden, in the Spanish Observatorio del Roque de los Muchachos of the Instituto de Astrofisica de Canarias.

References

Bartelmann, M. 1996, A&A, 313, 697

Beijersbergen, M., Hoekstra, H., van Dokkum, P. G., & van der Hulst, T. 2001, MNRAS, submitted [`astro-ph/0106354`]

Bertin, E., & Arnouts, S. 1996, A&AS, 117, 393

Blandford, R. D., & Narayan, R. 1992, ARA&A, 20, 311

Bonnet, H., Mellier, Y., & Fort, B. 1994, ApJ, 427, L83

Broadhurst, T. J., Taylor, A. N., & Peacock, J. A. 1995, ApJ, 438, 49 (BTP)

Broadhurst, T. J., Huang, X., Frye, B., & Ellis, R. 2000, ApJ, 534, L15 (B00)

Cohen, J., Hogg, D., Blandford, R., et al. 2000, ApJ, 538, 29

Coles, P., & Jones, B. 1991, MNRAS, 248, 1

Czoske, O., Soucail, G., Kneib, J.-P., et al. 1999, Gravitational Lensing: Recent Progress and Future Goals, Boston University, July 1999, ed. T. G. Brainerd, & C. S. Kochanek

Czoske, O., Kneib, J.-P., Soucail, G., et al. 2001a, A&A, 372, 391

Czoske, O., Moore, B., Kneib, J.-P., & Soucail, G. 2001b, A&A, submitted [`astro-ph/0111118`]

Dressler, A., & Gunn, J. E. 1992, ApJS, 78, 1

Dressler, A., Oemler, A., Couch, W. J., et al. 1997, ApJ, 490, 577

Dressler, A., Schneider, D. P., & Gunn, J. E. 1985, ApJ, 294, 70

Driver, S. P., Phillips, S., Davies, J. I., Morgan, I., & Disney, M. J. 1994, MNRAS, 268, 393

Dye, S., & Taylor, A. N. 1998, MNRAS, 300, L23

Fort, B., Mellier, Y., & Dantel-Fort, M. 1997, A&A, 321, 353

Fukugita, M., Shimasaku, K., & Ichikawa, T. 1995, PASP, 107, 945

Garilli, B., Maccagni, D., & Andreon, S. 1999, A&A, 342, 408

Ghigna, S., Moore, B., Governato, F., et al. 1998, MNRAS, 300, 146

Gray, M. E., Ellis, R. S., Refregier, A., et al. 2000, MNRAS, 318, 573

Hogg, D. W., Pahre, M. A., McCarthy, J. K., et al. 1997, MNRAS, 288, 404

Hudon, J. D., & Lilly, S. J. 1996, ApJ, 469, 519

Kaiser, N., Squires, G., & Broadhurst, T. 1995, ApJ, 449, 460

Kassiola, A., Kovner, I., & Fort, B. 1992, ApJ, 400, 41

Kinney, A. L., Calzetti, D., Bohlin, R. C., et al. 1996, ApJ, 467, 38

Kochanski, G. P., Dell' Antonio, I. P., & Tyson, J. A. 1996, A&AS, Meeting, 189, 73.02

Koo, D. C. 1988, in Large Scale Motions in the Universe, ed. V. C. Rubin, & G. V. Coyne (Princeton University Press), 513

Kovner, I. 1990, in Gravitational Lensing, ed. Y. Mellier, B. Fort, & G. Soucail (Springer), 16

Lin, H., Yee, H. K. C., Carlberg, R. G., et al. 1999, ApJ, 518, 533

Metcalfe, N., Shanks, T., Campos, A., McCracken, H. J., & Fong, R. 2001, MNRAS, 323, 795

Navarro, J. F., Frenk, C. S., & White, S. D. M. 1997, ApJ, 490, 493 (NFW)

Paolillo, M., Andreon, S., Longo, G., et al. 2001, A&A, 367, 59

Piranomonte, S., Paolillo, M., Andreon, S., et al. 2000, IAP Conf. Constructing the Universe with Clusters of Galaxies, Paris, July 2000

Pozzetti, L., Madau, P., Zamorani, G., Ferguson, H. C., & Bruzual, A. G. 1998, MNRAS, 298, 1133

Rögnvaldsson, Ö. E., Greve, T. R., Hjorth, J., et al. 2001, MNRAS, 322, 131 (R01)

Sandage, A., Tammann, G. A., & Yahil, A. 1979, ApJ, 232, 352

Schechter, P. 1976, ApJ, 203, 297

Schlegel, D., Finkbeiner, D., & Davis, M. 1998, ApJ, 500, 525

Schneider, P., Ehlers, J., & Falco, E. E. 1993, Gravitational Lenses (New York: Springer)

Smail, I., Hogg, D., Yan, L., & Cohen, J. 1995, ApJ, 449, L105

Smail, I., Dressler, A., Couch, W. J., et al. 1997, ApJ, 110, 213

Soucail, G., Ot, N., Böhringer, H., Czoske, O., Hattori, M., & Mellier, Y. 2000, A&A, 355, 433

Taylor, A. N., Dye, S., Broadhurst, T. J., Benitez, N., & van Kampen, E. 1998, ApJ, 501, 539 (T98)

Tyson, J. A., Kochanski, G. P., & Dell' Antonio, I. P. 1998, ApJ, 498, L107 (TKD)

van Kampen, E. 1998, MNRAS, 301, 389

Volonteri, M., Saracco, P., Chincarini, G., & Bolzonella, M. 2000, A&A, 362, 487

Wallington, S., Kochanek, C. S., & Koo, D. C. 1995, ApJ, 441, 58

Williams, R. E., Blacker, B., Dickinson, M., et al. 1996, AJ, 112, 1335

Wilson, G., Smail, I., Ellis, R. S., & Couch, W. J. 1997, MNRAS, 284, 915